Rapid cooling and exhumation as a consequence of extension and crustal thinning: Inferences from the Late Miocene to Pliocene Palu Metamorphic Complex, Sulawesi, Indonesia

Juliane Hennig [a,*], Robert Hall [a], Margaret A. Forster [b], Barry P. Kohn [c] and Gordon S. Lister [b]

[a] *SE Asia Research Group, Department of Earth Sciences, Royal Holloway University of London, Egham, TW20 0EX, UK*

[b] *Research School of Earth Sciences, The Australian National University, Canberra, ACT 0200, Australia*

[c] *School of Earth Sciences, University of Melbourne, Melbourne, VIC 3010, Australia*

* Corresponding author (email: juliane.hennig@rhul.ac.uk)

Abstract

Metamorphic complexes forming high mountains of 1.5-2 km in Western Sulawesi were previously considered to be Mesozoic or older basement of Gondwana crust. However, many of the metamorphic rocks are much younger than previously thought. Some have Eocene sedimentary protoliths. New geothermobarometric and geochronological data from metamorphic rocks of the Palu Metamorphic Complex (PMC) and associated granitoids provide information on the timing and mechanisms of Neogene metamorphism and contemporaneous rapid exhumation. The metamorphic rocks are strongly deformed and some were partially melted to form migmatites. Schists contain relict andalusite, cordierite, staurolite and Mn-rich garnet which are wrapped by a pervasive fabric. $^{40}Ar/^{39}Ar$ dating of biotite, white mica and amphibole from strongly deformed, mylonitic schists and recrystallised amphibolites reveals cooling occurred in the Early Pliocene (c. 5.3-4.8 Ma) in the northern part and during the Late Pliocene (c. 3.1-2.7 Ma) in the southern part of the PMC. U-Pb, $^{40}Ar/^{39}Ar$ and (U-Th)/He analyses of various minerals from PMC metamorphic and S-type magmatic rocks give very similar mid to Late Pliocene ages, indicating very fast cooling and rapid exhumation, and show the high speed at which tectonic processes, including magmatism, exhumation, and reworking into a sediment, must have occurred. The high rates could be unique to this area but we suggest they record the true speed of metamorphic complex exhumation in a very young orogenic belt. Rates in older orogens appear lower because they are averages measured over longer periods of time. Contemporaneous magmatism and deformation are interpreted as a consequence of decompressional melting due to extension and thinning of the crust, promoted by possible detachment faults and normal faulting at the major NW-trending Palu-Koro and Tambarana Faults. In contrast, I-type magmatic rocks, separated from the PMC by the Palu-Koro Fault, were exhumed from upper crustal levels by erosion at moderate rates.

Keywords: SE Asia; Palu Metamorphic Complex; rapid exhumation; cooling histories; $^{40}Ar/^{39}Ar$; (U-Th)/He

1. Introduction

Sulawesi is situated in a tectonically active convergent region between the Eurasian, Indo-Australian and Philippine Sea plates (Fig. 1). Recent studies have identified a major role for extension in the island's tectonic evolution during the Neogene (Spakman & Hall, 2010; Hall, 2011, 2012; Camplin & Hall, 2014; Hennig et al., 2014; Pownall et al., 2014) leading to the formation of deep basins between the four elongated land arms. Therefore, this area is of special interest as it allows us to study rocks which have formed very recently in the geological history and enable characterisation of the tectonic processes that drove cooling and exhumation.

The Neck of Sulawesi is a narrow strip of land that connects mid Central Sulawesi with the western end of the North Arm (Fig. 2a, b). It belongs to the Western Sulawesi province (Sukamto, 1975; Hamilton, 1979; Hall & Wilson, 2000; van Leeuwen & Muhardjo, 2005) which is underlain by Australian-origin continental basement (Jablonski et al., 2007; van Leeuwen et al., 2007; Cottam et al., 2011; Pholbud et al., 2012; Hall & Sevastjanova, 2012) that rifted from the Australian margin of Gondwana in the Late Jurassic and was added to the Sundaland margin in the Late Cretaceous (Smyth et al., 2007; Hall et al., 2009; Metcalfe, 2009; Hall, 2011, 2012; Hall & Sevastjanova, 2012; Hennig et al., 2016). Extension in the Eocene opened the Celebes Sea north of the island and led to rifting of the Makassar Straits, separating western Sulawesi from east Borneo (Hamilton, 1979; Weissel, 1980; Situmorang, 1982; Hall, 1996). Opening of the Makassar Straits has been attributed to back-arc rifting as a response to subduction rollback in SE Sundaland (Guntoro, 1999; Satyana, 2015).

The Neck forms the western boundary of the semi-enclosed Gorontalo Bay. High elevations of c. 1 to 2.5 km are observed on land all around Gorontalo Bay and contrast with significant depths in the bay (Fig. 2b) where there are sediment thicknesses of up to 6 s TWT (c. 6-10 km) and c. 1.5 - 2 km water depth (Jablonski et al., 2007; Pholbud et al., 2012). Shallow to deep marine sediments are found in the central North Arm in the Middle to Upper Miocene Dolokapa Formation (Bachri et al., 1993; Hennig et al., 2014; Rudyawan, 2015) as well as to the south of Gorontalo Bay in the central part of the island in the Pliocene Puna Formation (Simandjuntak et al., 1997) (Fig. 2a), indicating that the northern part of the island was largely a shallow marine area from the Middle Miocene, indicated by

widespread Middle Miocene carbonates exposed on land (Sukamto, 1973). Pinnacle reefs developed on top of carbonate platforms offshore mark subsidence associated with the onset of uplift in the area and indicate that mountain building must be a relatively young process in the tectonic history of the island (Pholbud et al., 2012; Pezzati et al., 2014). The youngest Plio- to Pleistocene clastic sediments of the Celebes Molasse in the southern Neck region (van Leeuwen & Muhardjo, 2005) unconformably overlie metamorphic rocks of the Palu Metamorphic Complex and contain zircons as young as 3 Ma which support a latest Pliocene to Pleistocene depositional age (Nugraha, 2016).

The high mountains on land are mainly formed by mid to lower crustal metamorphic rocks and granitoid intrusions. The timing and mechanisms of exhumation of these rocks are poorly known and investigated in this study by geothermobarometry, $^{40}Ar/^{39}Ar$ analysis and (U-Th)/He thermochronology.

2. Regional geology

Sulawesi is subdivided into five tectono-stratigraphic units (Fig. 2a) which are the Western Sulawesi magmatic belt, the Northern Sulawesi volcanic arc, the Central Sulawesi Metamorphic Belt, the East Sulawesi Ophiolite, and the micro-continental fragments of Banggai-Sula and Tukang Besi-Buton (Sukamto, 1975; Hamilton, 1979; Hall & Wilson, 2000; van Leeuwen & Muhardjo, 2005).

2.1 Metamorphic rocks

Metamorphic rocks are exposed at various places in Western Sulawesi (Fig. 2a), including the Malino Metamorphic Complex (MMC) in the western North Arm (Ratman, 1976; Kavalieris et al., 1992; van Leeuwen et al., 2007), the Palu Metamorphic Complex (PMC) in the Neck (Sukamto, 1973; van Leeuwen & Muhardjo, 2005; van Leeuwen et al., 2016), and the Gumbasa, Wana and Karossa Metamorphic Complexes to the east and west side of the Palu-Koro fault zone (Ratman & Atmawinata, 1993; Sukido et al., 1993; Calvert & Hall, 2003; van Leeuwen & Muhardjo, 2005). Metamorphic rocks were described from the Tokorondo and Pompangeo Metamorphic Complexes in the Central Sulawesi Metamorphic Belt (Simandjuntak et al., 1991, 1997; Parkinson, 1998). The PMC comprises chlorite- and biotite-schists, paragneisses, granite-gneisses, amphibolites, marbles, and subordinate granulites, eclogites and peridotites (Egeler, 1947; Sukamto, 1973; van Leeuwen & Muhardjo, 2005).

2.1.1 Age and origin of the metamorphic rocks

The metamorphic rocks of Western Sulawesi have been interpreted as Mesozoic basement rocks (Parkinson, 1998; Calvert & Hall, 2003; van Leeuwen & Muhardjo, 2005). They were assigned to different metamorphic complexes based on differences in the proposed protolith ages, e.g. Permo-Triassic for the PMC (van Leeuwen & Muhardjo, 2005) and Triassic to Jurassic for the Gumbasa Metamorphic Complex (Sukido et al., 1993), implying a different origin and/or tectonic evolution for the fragments.

Petrographic observations of schists and gneisses of the metamorphic rocks of the PMC and smaller complexes in mid Central Sulawesi in this study reveal similar lithologies which differ only in the proportion and intensity of deformation. Zircon U-Pb dating of these rocks identified comparable detrital zircon age populations, indicating similar protoliths for the metamorphic rocks in different areas which may form part of a single metamorphic complex (Hennig et al., 2016).

Recently, metamorphic rocks of the PMC were dated as Late Miocene to Pliocene by zircon U-Pb geochronology and mica, K-feldspar and hornblende $^{40}Ar/^{39}Ar$ analysis (van Leeuwen et al., 2016). Pliocene metamorphism (c. 3.6 Ma) was also confirmed by U-Pb age dating of zircon rims from biotite- and biotite-amphibole gneisses of the eastern side of the southern Neck near Toboli (Hennig et al., 2016).

2.2 Paleogene (meta-) sedimentary rocks

Sedimentary and low-grade metasedimentary rocks are abundant to the north of the PMC in the Neck (Fig. 2a) and were assigned to the Tinombo Formation (Ahlburg, 1913; Brouwer, 1934; Sukamto, 1973; Ratman, 1976; Apandi, 1977; van Leeuwen & Muhardjo, 2005). The sedimentary sequence comprises mudstone, sandstone, conglomerate, arkose, nummulitic limestone, radiolarian chert, marl, greywacke, quartzite, slate and phyllite, as well as subordinate felsic/intermediate to basic volcanic and plutonic rocks (Ahlburg, 1913; Brouwer, 1934; Sukamto, 1973; Ratman, 1976; Elburg et al., 2003; van Leeuwen & Muhardjo, 2005).

The timing of deposition is poorly known and based on limited paleontological evidence from pelagic carbonates and nummulitic limestones of Eocene age (Brouwer, 1934; Sukamto, 1973; van Leeuwen & Muhardjo, 2005). Similar Late Eocene magmatic zircon ages were acquired from a schist of the PMC and interpreted as inherited ages of detrital zircons, indicating that these rocks probably

represent the metamorphosed equivalents of Paleogene sedimentary rocks (Hennig et al., 2016; van Leeuwen et al., 2016).

Biotite hornfels is locally exposed within the low-grade (meta-) sedimentary rocks of the Tinombo Formation, as well as in the PMC metamorphics, and was interpreted as the product of high-temperature contact metamorphism during widespread Neogene magmatism (van Leeuwen et al., 1994).

2.3 Neogene magmatic rocks

Widespread Neogene intrusives and extrusives in Western Sulawesi were classified as high-K ultrapotassic, alkaline and shoshonitic rocks (HK suite) or high-K calc-alkaline rocks (CAK suite) (Priadi et al., 1994; Polvé et al., 1997; Elburg et al., 2003). K-Ar ages reported from whole-rocks, micas, and feldspars have wide ranges of 13-10 Ma (Priadi et al., 1994; Polvé et al., 1997) or 14-5 Ma (Elburg et al., 2003) for the HK suite, and 6.5-0.6 Ma (Priadi et al., 1994; Polvé et al., 1997) or 9-2 Ma for the CAK suite (Elburg et al., 2003). U-Pb zircon dating defines a Late Miocene to Pliocene age (8.5 to 4 Ma) for I-type and silica-rich I-type group of mainly CAK magmatic rocks, and a Pliocene age (5 to 2.5 Ma) for an S-type group (Hennig et al., 2016).

The cooling histories of the magmatic rocks have been little studied. Bellier et al. (2006) reported apatite, titanite and zircon fission-track ages from granitoids west of the Palu-Koro Fault ranging from 2.1 to 6.6 Ma. A phase of rapid cooling was identified between 4.1 and 3.3 Ma at a rate of >300°C/Ma, interpreted to reflect regional uplift and increased erosion due to the collision of the Banggai-Sula micro-continent, as well as normal faulting along the Palu-Koro Fault (Bellier et al., 2006). Below c. 60°C cooling slowed to a rate of 12°C/Ma as a consequence of uplift and erosion of the uppermost part of the continental crust (Bellier et al., 2006). Exhumation rates of 0.65 - 1 mm/yr were estimated from these granitoids by Bellier et al. (2006) based on a biotite K-Ar age of 7.7 ± 0.2 Ma reported by Elburg et al. (2003).

Maulana et al. (2013) calculated exhumation rates from intrusion depth estimates using the aluminium-in-hornblende geobarometer of Anderson & Smith (1995) and $^{40}Ar/^{39}Ar$ ages of 4.3 Ma to 9.5 Ma. The exhumation rates reported vary between relatively high rates of 2.7 mm/yr and 1.6 mm/yr for the Soni and Masamba plutons and low rates of 0.4 mm/yr for the Mamasa pluton.

2.4 Celebes Molasse

The Celebes Molasse (Sarasin & Sarasin, 1901; van Bemmelen, 1949) forms large packages of clastic sediments on the west side of the southern Neck (Sukamto, 1973). The northern section was described as dominated by limestones and marls, containing foraminifera of Miocene age (Sukamto, 1973). Van Leeuwen & Muhardjo (2005) determined a Pleistocene depositional age based on nannofossils and a K-Ar age of c. 1.7 Ma obtained from alunite clasts in the sediments. Granitoid boulders observed in the Celebes Molasse in this study are similar to nearby plutons of Late Miocene to Pliocene age, indicating that exhumation as well as reworking into the sediment took place very recently and rapidly.

3. Methodology

Five metamorphic and 19 granitoid samples from fresh and mainly unaltered rocks were sampled from the Neck and mid Central Sulawesi in this study and analysed by geothermobarometry, $^{40}Ar/^{39}Ar$ and/or (U-Th)/He thermochronology.

3.1 Mineral chemical analyses

Electron microprobe mineral chemical analyses was obtained from biotite and garnet from metamorphic rocks using energy-dispersive spectroscopy (EDS), and on biotite from magmatic rocks using wavelength-dispersive spectroscopy (WDS) (Supplementary Files 1 and 2). Analyses were performed on carbon-coated polished thin sections at UCL/Birkbeck College. Single spot analysis was carried out on a JEOL JXA-8100 Superprobe which is coupled to an Oxford Instruments INCA system using an accelerating voltage of 15 kV, a beam current of 2.5 µA, and a beam diameter of 1 µm. Standard natural silicates, oxides, and Specpure metals were used for calibration. Data correction was performed using a ZAF algorithm.

Garnet end members were calculated using a Pascal program (FORMULA written by R. Hall) which estimates Fe^{3+} based on an ideal composition of 24 oxygens and 16 cations.

3.2 Geothermobarometry

3.2.1 Ti-in-biotite geothermometer

The Ti-in-biotite thermometer of Henry et al. (2005) was used for temperature estimates of schists from the PMC. This method is proposed for graphitic peraluminous metapelites that contain ilmenite or rutile (= excess Ti). Errors of ± 24°C were reported for low temperatures (480-600°C).

3.2.2 Aluminium-in-hornblende geobarometer

Pressure and temperature conditions were calculated for two Neogene I-type rocks (SJH07; SJH11_46) using the temperature-dependent geobarometer of Anderson & Smith (1995) which includes the plagioclase-hornblende geothermometer of Holland & Blundy (1994).

3.3 Geochronology

3.3.1 $^{40}Ar/^{39}Ar$ analysis

Analysis of different potassium-rich minerals can be used to study the cooling history of a rock and/or recrystallisation during deformation or heating events. However, the closure temperatures of different systems are not fixed values but a variable temperature range that can be dependent on the grain size or the cooling rate (Dodson, 1973; Harrison, 1981; Harrison et al., 1985, 2005) and variation in chemical composition (e.g. Forster & Lister, 2014).

$^{40}Ar/^{39}Ar$ analysis was carried out by incremental heating of the sample and enables examination of the argon release behaviour. Rocks with a complex metamorphic history are considered to comprise multiple diffusion domains (MDD) which include more retentive domains that may not have been completely reset during recrystallisation (Lovera et al., 1989, 1991). Multiple generations of one mineral can also represent different sources of radiogenic argon (Wijbrans & McDougall, 1986; Forster & Lister, 2004, 2014). Therefore, thorough microstructural and microchemical analysis needs to be carried out for grain selection prior to analysis and apparent age spectra interpretation.

3.3.1.1 Sample analysis and data interpretation

Mineral separation for $^{40}Ar/^{39}Ar$ analysis was carried out at Royal Holloway University of London, UK and prepared for irradiation at the Research School of Earth Sciences at The Australian National University (ANU) in Canberra. Mineral separates from the metamorphic rocks from canister ANU#13 were sent to the USGS TRIGA Nuclear Reactor in Denver (USA) and irradiated with the GA1550

biotite standard (98.5 ± 0.8 Ma; Spell & McDougall, 2003). Samples from the magmatic rocks from canister ANU#7 were irradiated at the McMaster Nuclear Reactor in Ontario (Canada) with the Fish Canyon Tuff sanidine standard (28.10 ± 0.04 Ma; Spell & McDougall, 2003) that was used as a reference.

Sample analysis and data reduction were performed in the Argon Geochronology Facility at the Research School of Earth Sciences, ANU. The samples were incrementally heated using a double-vacuum resistance furnace for gas extraction and a single collector VG1200 gas-source mass spectrometer was used for analysis. The data were reduced using the software *Noble v1.8*. The measured Ar isotope concentrations are displayed for each heating step in the Supplementary File 3. Data interpretation was carried out with the programme *eArgon* written by G. S. Lister using the approach described by Forster & Lister (2004), Beltrando et al. (2009) and Pownall et al. (2014). P-values (probabilities) shown with the data were calculated using Isoplot 4.15 (Ludwig, 2003).

The data were visually assessed in the Arrhenius plot, as well as in the log (r/r_0) plot to identify distinct argon domains during the heating process which are used to infer closure temperature estimates (Forster & Lister, 2004, 2010). Closure temperatures indicated for the initial and final heating steps are also shown with the data to give some constraints for the possible range, however they were not further considered as they are related to high atmospheric argon contents, excess argon or grain disintegration. The full analysis of the Ar data is compiled in the Supplementary File 4, including the York plot (inverse isochron between the atmospheric and radiogenic argon), and the Ca/K and Cl/K ratio profiles (Forster & Lister, 2004, 2010). Flat plateaux with only minor loss indicated by the first heating steps are considered as an indication of closed systems, and are interpreted as undisturbed by locally observed retrograde metamorphism.

3.3.2 (U-Th)/He thermochronology

The (U-Th)/He method is based on alpha-particle decay from parent radiogenic isotopes. Above temperatures of c. 70°C for apatites and c. 180°C for zircons diffusion of alpha-particles is high enough to remove all helium from the system (Wolf et al., 1996; Farley, 2000; Ehlers & Farley, 2003; Reiners et al., 2004). If a rock cools below that temperature, helium starts to accumulate and can be measured and used to determine the time that has elapsed since the rock cooled below the closure temperature. This provides valuable insights into the cooling and exhumation histories through the uppermost part of the continental crust.

3.3.2.1 Sample analysis and data interpretation

Apatites and zircons were separated from granitoid rocks sampled from the Neck region and from the areas east and west of the Palu-Koro Fault. Mineral separation and grain selection for analysis, including grain size, inclusion content, and geometry (degree of grain preservation) was carried out at Royal Holloway University of London, UK.

Sample analysis was performed at the University of Melbourne, Australia using a solid-state diode laser for helium extraction coupled to a Balzers quadrupole mass spectrometer. For details of analytical methods see Gleadow et al. (2015). The Durango fluorapatite ((U-Th)/He age: 31.02 ± 1.01 Ma; McDowell et al., 2005) was used as a standard for calibration.

A triplicate single grain analysis was usually performed unless the helium gas concentration was too low, in which case two to four grains were combined in one analysis. The grain parameters, including radius, geometry, alpha-ejection correction and effective U concentration (eU), as well as the number of grains per analysis and the age results are summarised in Tables 1.1 and 1.2.

Aliquot apatite analyses from different samples across the study area yielded variable ages. Within the same sample analyses often showed poor reproducibility which in many instances appeared to yield excess (U-Th)/He ages. Age differences between grains from the same sample has often been observed in (U-Th)/He thermochronometry and has been attributed to a number of possible factors. These include undetected U and/or Th-rich micro-inclusions, zonation in U and Th content, grain size variation, He implantation from external source, effects from radiation damage, or grain breakage (e.g. Fitzgerald et al., 2006; Shuster et al., 2006; Spiegel et al., 2009; Brown et al., 2013). Therefore, our results were evaluated based on their plausibility (i.e. when compared to ages obtained by U-Pb and $^{40}Ar/^{39}Ar$ geochronology and excluded from further discussion if the (U-Th)/He age was older than the crystallisation age), as well as reproducibility to test if they form outliers compared to other aliquot analysis of the same sample or from another sample of the same area. Samples SJH11_22 and SJH11_100 have widely dispersed ages (Table 1.1) which were disregarded.

Complete and incomplete grains were assumed to have flat diffusion profiles based on the young (U-Th)/He ages and similar $^{40}Ar/^{39}Ar$ and U-Pb zircon ages, indicating rapid exhumation and therefore an undisturbed accumulation of helium. The effective U concentrations calculated for apatites and zircons do not correlate with age differences (Tables 1.1 and 1.2).

4. Lithologies

4.1 Palu Metamorphic Complex

The Palu Metamorphic Complex is generally divided into a metapelite unit on the west side of the complex and a gneiss unit on the east side (Sukamto, 1973; van Leeuwen & Muhardjo, 2005). Rocks observed in the field showed the latter comprises mainly high-grade metamorphic rocks, including biotite granite-gneisses and biotite-amphibole granite-gneisses, and subordinate pyroxene gneisses, marbles and migmatites. Gneisses and marbles are recumbently folded with tight to isoclinal folds at centimetre- to several metres-scale. To the west the metamorphic grade decreases and foliated biotite schists and biotite - white mica schists are dominant and are interbanded with amphibolites in places.

4.1.1 Biotite (- white mica) schists

Schists of the PMC were collected from the Tawaeli – Toboli traverse, as well as from exposures at rivers near Oti and Tompe (Fig. 2b). They are strongly foliated, classified as mylonitic after Passchier & Trouw (2005), and composed of quartz, feldspar, biotite ± white mica ± garnet ± andalusite ± cordierite ± staurolite ± tourmaline ± graphite and ilmenite.

SJH11_16: andalusite cordierite schist

The rock consists of fine-grained quartz, feldspar and biotite forming a strong foliation which contains folded quartz lenses of coarse- to medium-grained quartz with irregular grain boundaries and bulging structures from dynamic recrystallisation. The sample contains large andalusite porphyroblasts of c. 2 to 5 mm in length (Fig. 3a), as well as cordierite porphyroblasts wrapped around by the strongly recrystallised mylonitic fabric. Subidioblastic andalusite and subidioblastic to xenoblastic cordierite crystals are pre-kinematic and have abundant aligned biotite inclusions that represent an earlier foliation oblique to the dominant foliation (Fig. 3b, c). There is a second generation of idioblastic andalusite crystals which grew syn-kinematically with the dominant foliation and show no internal fabric. Locally, biotite and fibrolitic sillimanite have grown along small shear planes which cut the foliation planes and form an SC shear fabric. Cordierite is locally altered to pinite (Fig. 3d). Hypidiomorphic white mica grew at the rims of some porphyroblasts during retrograde metamorphism.

PMC06: andalusite cordierite staurolite schist

The sample was collected c. 150 m from SJH11_16 at the roadside between Tawaeli and Toboli. The mylonitic schist is fine-grained and strongly foliated (Fig. 3e). Andalusite porphyroblasts of <1 to 5 mm in length are abundant and surrounded by biotites of the foliation planes (Fig. 3e). Some andalusite crystals contain thin quartz bands and biotite flakes oblique to the dominant fabric, representing remnants of an earlier foliation. Rarely, small staurolite crystals were observed which are either in contact with andalusite (Fig. 3f) or in the quartz pressure shadow of an andalusite, and are also wrapped around by biotite of the foliation planes. Xenoblastic cordierite crystals were observed in bands with xenomorphic biotite (Fig. 3g, h). Like sample SJH11_16, the foliation is locally cut by small shear bands of biotite and fibrolitic sillimanite (Fig. 3g, h). Locally, cordierite is partly replaced by white mica, and biotite partly by chlorite, recording retrograde metamorphism.

A float sample (SJH32) collected from a nearby river also has a strongly foliated, mylonitic fabric and a very similar mineral assemblage of quartz, feldspar, biotite, andalusite porphyroblasts, pinite pseudomorphs after cordierite with retrograde growth of white mica (Fig. 4a, b), and staurolite which is rimmed and partly replaced by white mica (Fig. 4c). The foliation is cut by shear bands of biotite and subordinate white mica.

SJH11_1214: garnet schist

The sample was collected c. 2 km from samples SJH11_16 and PMC06 between Tawaeli and Toboli. The fine-grained rock contains coarse-grained quartz lenses and is mainly composed of quartz, feldspar and biotite forming a foliation which is locally folded and cut by thin shear bands. Garnet porphyroblasts (c. 0.5 – 1.0 mm in length) are surrounded by the foliation. Some garnets show aligned biotite inclusions oblique to the foliation which indicates they were formed during an earlier event (Fig. 4d).

SJH11_31: cordierite schist

The rock was sampled from the banks of the river Alindau near Oti. It is a fine-to medium-grained mylonitic schist with quartz-rich and biotite - white mica bands. The sample contains xenoblastic cordierite grains which are partly altered to pinite (Fig. 4e). The foliation is cut by thin shear bands of biotite and white mica (Fig. 4f).

PMC09: garnet andalusite cordierite schist

The sample was collected from an outcrop at a river near Tompe. The fine-grained schist contains abundant quartz lenses within strongly foliated quartz and feldspar with biotite and white mica

362 which is locally altered to sericite (Fig. 5a, b). Locally, the foliation is cut by small shear bands of
363 mica/sericite and subordinate fibrolitic sillimanite. Andalusite, cordierite, which is partly or
364 completely altered to pinite, and garnet porphyroblasts formed during an early event and are
365 wrapped around by the foliation (Fig. 5c, d). Subordinate medium-grained biotite, some intergrown
366 with white mica, is oblique to the foliation. Biotite is also observed in contact with andalusite (Fig.
367 5c) and pinite pseudomorphs after cordierite (Fig. 5e-g), and therefore considered to represent part
368 of a stable mineral assemblage with andalusite, cordierite and garnet porphyroblasts. Andalusite, as
369 well as cordierite, are rimmed and partially replaced by hypidioblastic white mica formed during
370 retrograde metamorphism (Fig. 5c, e).
371
372 ***4.1.2 Amphibolites***
373 Amphibolites are locally interbanded with the schists or form irregular lenses (c. 5-20 m in length)
374 (Fig. 6a). They have sharp contacts, representing original dyke margins or tectonic contacts. The
375 rocks are composed of plagioclase, amphibole, quartz ± spinel ± clinozoisite ± allanite ± calcite ±
376 titanite and an opaque phase. Textures vary from relatively undeformed to foliated and strongly
377 deformed mylonitic rocks which contain plagioclase or amphibole porphyroclasts (Fig. 6b).
378
379 *SJH11_17: amphibolite*
380 The rock was sampled from an amphibolite body within the schists of the PMC at the roadside
381 between Tawaeli and Toboli. The amphibolite is deformed and has sharp contacts with the schists.
382 Thin section analysis shows a fine-grained recrystallised texture of amphibole, plagioclase and quartz
383 with retrograde clinozoisite and accessory titanite and allanite (Fig. 6c, d). Amphibole forms a weak
384 cleavage around plagioclase porphyroclasts or recrystallised pseudomorphs.
385
386 **4.2 S-type granitoids**
387 S-type granites, including multiple generations of moderately to steeply dipping and strongly
388 fractured dykes with cross-cutting relationships, have intruded the schists and gneisses of the PMC
389 (Fig. 7a). Some dykes show irregular contacts or dyke boudinage subparallel to the low-angle NW-
390 dipping schist foliation planes (Fig. 7b). The S-type (CAK) granitoids continue to the south of PMC
391 where they are part of the very similar Gumbasa and Wana Metamorphic Complexes east of the
392 Palu-Koro Fault (Hennig et al., 2016).
393
394 *SJH01: Biotite granite dyke*

The rock is exposed at the roadside between Tawaeli and Toboli. It shows a medium-grained magmatic texture with no orientation. The granite is composed of quartz, K-feldspar, plagioclase, hypidiomorphic and xenomorphic biotite, and subordinate white mica and ilmenite (Fig. 7c). Evidence of minor deformation include dynamic recrystallisation of quartz forming bulging structures and quartz subgrains and new grains.

SJH30: Biotite granite

The sample was collected from a small boulder field southeast of the Palolo Basin. The undeformed rock is composed of quartz, K-feldspar, zoned plagioclase with dark cores and light rims, and medium-grained hypidiomorphic and xenomorphic biotite flakes (Fig. 7d).

4.3 I-type magmatic intrusions

In contrast to the S-type granitoids, magmatic rocks with I-type affinities are predominant to the west of the Palu-Koro Fault and along the west side of the Neck (Hennig et al., 2016). They intruded hypabyssal basaltic rocks which represent higher crustal levels than the mid-crustal metamorphic complexes east of the fault (Fig. 8).

SJH03: Granodiorite

The granodiorite intrusion crops out on the western side of the Neck near Tambu. It has a coarse-grained un-oriented magmatic texture and consists of quartz, oscillatory zoned plagioclase, K-feldspar, hypidiomorphic to idiomorphic biotite and hornblende, titanite and magnetite (Fig. 7e, f). Some biotite crystals show minor retrograde chlorite alteration at the rims. Minor evidence of deformation includes some quartz grains with undulose extinction.

SJH07: Diorite

Diorites are exposed in the high mountains to the west of the Palu valley (Fig. 2b). The undeformed rocks are composed of quartz, plagioclase, K-feldspar, hypidiomorphic and xenomorphic biotite flakes, amphibole crystals which are up to 2 cm in length (some with clinopyroxene cores), and magnetite. Locally, the rocks are deformed in small shear zones, or show elongated or deformed mafic enclaves (Fig. 7g). In thin section, quartz is often undulose and shows locally evidence of dynamic recrystallisation by subgrain formation and grain boundary migration.

SJH08: Granodiorite

The undeformed granodiorite is exposed in the high mountains to the west of the Palu valley near Baluase (Fig. 2b). It consists of large pink K-feldspar phenocrysts to megacrysts (up to 4 cm in length), quartz, oscillatory zoned plagioclase, and hypidiomorphic biotite and amphibole (some with relict clinopyroxene cores) and magnetite. Quartz shows minor evidence of deformation indicated by irregular grain boundaries from dynamic recrystallisation. Some biotites have chlorite growth at rims. The rocks are strongly fractured, which can also be observed at cm-scale in K-feldspar crystals (Fig. 7h).

SJH11_46: Granodiorite

A coarse-grained granodiorite is exposed at the west side of the northern Neck south of Soni (Fig. 2b). It has an equigranular phaneritic texture composed of quartz, plagioclase, K-feldspar, hypidiomorphic biotite, hypidiomorphic and idiomorphic amphibole and magnetite. Biotite is partly replaced by chlorite; amphibole rarely by epidote and chlorite.

5. Structural analysis

Structural data is summarised on stereonets (Fig. 9a, b) and in a sketch box model (Fig. 9c).

5.1 Ductile deformation

Foliation orientations of biotite - white mica schists of the northern PMC vary widely due to intense folding. They dip at moderate angles predominantly to the E or NE and subordinately to the SE and SW. Subordinate stretching lineations vary in their orientation from approximately northward (NW to N) to E-, SE-, and W-directed with plunges at low to moderate angles (Fig. 9a).

Biotite schists in the southern PMC have a strong foliation and contain folded or boudinaged quartz veins (Fig. 9d) and boudinaged granitic dykes (Fig. 7b). The foliation of the mylonitic schists in shear zones dips at low to moderate angles to the WNW and NW, and subordinately to the N or NE (Fig. 9b). Mineral stretching lineations plunge predominantly to the W or SW.

Mylonitised biotite hornfels (Fig. 9e) of the Tinombo Formation was abundant in float east of Sabong (Fig. 2b), and SC shear fabrics (Fig. 9f) were observed in slates north of the Sabong, indicating top to the north movement.

5.2 Brittle deformation

Field observations and shuttle radar topography mission (SRTM) images were used to identify three major fault trends: N-S to NNW-SSE strike-slip faults, WNW-ESE to NW-SE normal or reverse faults, and NE-SW faults (Fig. 2a).

The first group includes the active major NNW-trending transtensional Palu-Koro Fault and a sub-parallel Tambarana Fault, largely offshore, that bounds the PMC to the east (Pholbud et al., 2012). Within the PMC only minor strike-slip faults were observed with steep dips and variable NNE to NE-trending orientations, possibly forming flower-structures. Riedel shears indicate a sinistral movement direction and striae on the fault planes plunge to the NE at low angles (Fig. 9c).

Minor N- to NE-dipping normal faults and transtensional strike-slip faults cut through the rocks at low to medium angles (Fig. 9g).

6. Chemistry and geothermobarometry

6.1 Biotite of metamorphic rocks/ Ti-in-biotite geothermometer

SJH11_1214:

Two different kinds of biotites were identified in this sample (Supplementary File 1). The first generation forms inclusions in garnet porphyroblasts (Biotite 1) and is assumed to be in equilibrium with the garnet, while the second generation of biotite represents flakes of the surrounding foliation (Biotite 2). A representative analysis of Biotite 1 has 2.11 wt% TiO_2 and a Mg-number of 0.51. Biotite 2 has 2.65 and 2.73 wt% TiO_2 and Mg-numbers of 0.48 and 0.49. The Ti-in-biotite geothermometer estimates temperatures of 622 ± 24°C for Biotite 1, and 656 and 669 ± 24°C for Biotite 2 which are similar within error.

PMC09:

Two representative biotite analyses from relict biotite flakes between foliation planes had 1.47 and 1.96 wt% TiO_2, and Mg-numbers of 0.44 which equates to temperatures of 554 and 615 ± 24°C.

6.2 Garnet of metamorphic rocks

Garnet was observed in thin sections of the metamorphic samples SJH11_1214 and PMC09 and analysed by electron microprobe (Supplementary File 1).

492

493 *SJH11_1214:*

494 Several analysis spots were acquired across the garnets which indicated homogeneous
495 compositions. They are Mn-rich almandine garnets with dominant almandine (58-62 %), minor
496 pyrope (14-18 %) and spessartine (13-17 %), and subordinate grossular (0-6 %), andradite +
497 schorlomite (1-11 %) and uvarovite (0.0-0.4 %).

498

499 *PMC09:*

500 The garnets are unzoned and homogeneous based on several analysis spots. They are also Mn-rich
501 almandine garnets with dominant almandine (55-56 %), minor spessartine (26-28 %), and
502 subordinate pyrope (8-9 %), andradite + schorlomite (9 %) and uvarovite (0.0-0.2 %).

503

504 **6.3 Biotite of magmatic rocks (I-and S-type granitoids)**

505 Chemical compositions of biotites from four granitoids analysed by $^{40}Ar/^{39}Ar$ analysis (SJH01, SJH03,
506 SJH08, SJH30) were determined using electron microprobe WDS (Supplementary File 2). Biotites of
507 samples SJH03 and SJH08 are meroxene (X_{Fe} = 43-47), and lepidomelane to subordinate meroxene
508 (X_{Fe} = 47-66) for samples SJH01 and SJH30, (Supplementary File 5) based on the classification of Deer
509 et al. (1962) and Tröger (1982). All biotites are homogeneous as indicated by several analysis spots
510 which were obtained from different places of the flakes.

511

512 Biotites from the I-type samples SJH03 and SJH08 have very similar compositions. Compared to
513 them, the biotites from the S-type samples SJH01 and SJH30 have higher Al_2O_3, FeOt, MnO and F
514 contents, and lower MgO, TiO_2, Cr_2O_3 and BaO contents.

515

516 **6.4 Al-in-hornblende geobarometer (I-type magmatic rocks)**

517 Chemical analyses of hornblende and plagioclase (Supplementary File 1) in a diorite from the west
518 side of the Palu-Koro Fault (SJH07) and a granodiorite from the northern Neck near Soni (SJH11_46)
519 were used to determine the P-T conditions of crystallisation.

520

521 Both samples are classified as I-type rocks and composed of quartz, plagioclase, K-feldspar, biotite,
522 hornblende, titanite and magnetite, which is a suitable assemblage for the aluminium-in-hornblende
523 barometer of Anderson & Smith (1995). Temperature estimates used in the calculation are based on
524 the plagioclase-hornblende thermometer of Holland & Blundy (1994) and are c. 700°C for sample

SJH07 and c. 680°C for sample SJH11_46 from representative microprobe analyses. These yield pressure estimates of 1.7 ± 0.6 kbar (SJH07) and 2.0 ± 0.6 kbar (SJH11_46) which equate to depths of c. 6.2 and 7.3 ± 2.2 km respectively, assuming an average density of 2.8 g/cm^3 for the continental crust (Taylor & McLennan, 1997).

7. $^{40}Ar/^{39}Ar$ dating

7.1 Palu Metamorphic Complex

Amphibole, white mica and biotite were separated from biotite (- white mica) schists and an interbanded amphibolite of the PMC. The minerals analysed were separated from the dominant metamorphic fabric which has mainly overprinted older fabrics.

7.1.1 Biotite-white mica schist - SJH11_31

White mica

The age spectrum shows a plateau at 5.27 ± 0.13 Ma (MSWD = 25.69) that degassed c. 75 % of the total ^{39}Ar released (Fig. 10a). The Ca/K ratio shows only some contamination for the initial and final heating steps, and the Cl/K ratio is very flat throughout the analysis, indicating only minor contamination (Supplementary File 4). The plateau consists of asymptotically increasing apparent ages. The first three steps of the plateau were accessed at 750-850°C and contain high proportions of radiogenic argon as shown in the York plot (Supplementary File 4), indicating cooling through c. 368°C in the Arrhenius plot, while the following heating steps of the plateau indicate some mixing which is confirmed in the $\log_{10}(r/r_0)$ and Arrhenius plots (Fig. 10b, c).

Biotite

The age spectrum shows a flat plateau at 4.84 ± 0.09 Ma (MSWD = 24.87) for the heating steps 7 to 16 which degassed c. 80 % of the total ^{39}Ar released (Fig. 10d). They were accessed at 680-1000°C and have the highest radiogenic argon contents in the York plot with very low Ca/K and Cl/K ratios (Supplementary File 4), indicating very minor, negligible contamination. The steps 7 to 12 indicate mixing in the $\log_{10}(r/r_0)$ and Arrhenius plots (Fig. 10e, f), while the last four steps of the plateau form a domain indicating cooling through c. 376°C.

7.1.2 Recrystallised amphibolite - SH11_17

The age spectrum shows a moderately well-defined plateau at 3.05 ± 0.05 Ma (MSWD = 6.32) that degassed c. 90 % of the total ^{39}Ar released (Fig. 10g). The Ca/K ratio is relatively high throughout the analysis which may be related to compositional variations or some contamination, however, the Cl/K

ratio is low and shows only minor contamination for the initial and final heating steps (Supplementary File 4).

The plateau is defined by the three heating steps 7, 10 and 13 (accessed at 800-1000°C), although two additional steps of the plateau (11 and 12) could be included in the age calculation which would only result in a slight change of age (c. 3.2 Ma) but includes a larger error. The York plot shows high proportions of atmospheric argon, however, the steps selected contain high radiogenic argon contents (Supplementary File 4). The steps 7 to 9 (800-866°C) form a domain which indicate cooling through c. 568°C, while steps 11 to 13 show some mixing in the $\log_{10}(r/r_0)$ and Arrhenius plots (Fig. 10h, i).

7.1.3 Biotite schist – SJH32

The age spectrum shows a very flat age plateau at 2.70 ± 0.11 Ma (MSWD = 25.91) which degassed c. 80 % of the ^{39}Ar released (Fig. 10j). The Ca/K and Cl/K ratios are very low and show only minor contaminations (Supplementary File 4). The plateau is formed by the heating steps 7 to 16 (excluding step 8 as an outlier) which were accessed at 666-1000°C. They contain the highest radiogenic argon contents based on the York plot (Supplementary File 4). Some show mixing in the $\log_{10}(r/r_0)$ and Arrhenius plots (Fig. 10k, l), while steps 12 and 13 form a domain which is related to cooling through c. 404°C.

7.2 S-type granitoids

Biotites were analysed from a granite dyke within the PMC sampled between Tawaeli and Toboli (SJH01), and from float collected south of the PMC, southeast of the Palolo Basin (SJH30). Samples selected have an un-oriented magmatic texture and show little or no alteration.

7.2.1 Granite dyke (SJH01) – Neck region

The age spectrum shows a very flat plateau at 3.12 ± 0.05 Ma (MSWD = 0.97) which degassed c. 90 % of the total ^{39}Ar released (Fig. 11a). The Ca/K and Cl/K ratios are very low and show only minor contaminations (Supplementary File 4). The heating steps 6 to 16 of the plateau were accessed at 750-1100°C and plot along an inverse isochron between the radiogenic and atmospheric argon compositions in the York plot (Supplementary File 4) which results in mixing, also evident in the $\log_{10}(r/r_0)$ and Arrhenius plots (Fig. 11b, c). Steps 11 and 12 form a domain that indicates rapid cooling through c. 464°C.

7.2.2 Granite (SJH30) – South of the Neck, mid Central Sulawesi

The age spectrum shows a flat plateau at 3.27 ± 0.08 Ma (MSWD = 6.97) which degassed c. 85 % of the total ^{39}Ar released (Fig. 11d). The Ca/K is very low and the Cl/K ratios shows some minor contamination (Supplementary File 4). The plateau consists of the heating steps 6 to 14 which were accessed at 750-1030°C. Steps 6 to 10 show mixing in the $\log_{10}(r/r_0)$ and Arrhenius plots (Fig. 11e, f), while steps 11 to 14 form a domain which is related to rapid cooling through 480°C as indicated from the Arrhenius plot (Fig. 11f).

7.3 I-type magmatic intrusions

Two biotite samples from I-type rocks from the southern Neck (SJH03) and west side of the Palu-Koro Fault (SJH08) were analysed. They have an un-oriented magmatic texture and show little alteration.

7.3.1 Granodiorite (SJH03) – Neck region

The age spectrum shows a flat plateau at 7.15 ± 0.11 Ma (MSWD = 6.33) that degassed c. 90 % of the total ^{39}Ar released (Fig. 11g). The Ca/K and Cl/K ratios show low contaminations (Supplementary File 4) which may be due to some chlorite overgrowth. The plateau is formed by the heating steps 8 to 17 which were accessed at 790-1120°C. The steps 8 to 14 show some mixing in the $\log_{10}(r/r_0)$ and Arrhenius plots (Fig. 11h, i), while the last three steps of the plateau contain the highest radiogenic argon contents based on the York plot (Supplementary File 4) and form a domain related to rapid cooling through 465°C (Fig. 11i).

7.3.2 Granodiorite (SJH08) – Mid Central Sulawesi

The age spectrum shows a flat plateau at 6.40 ± 0.11 Ma (MSWD = 9.95) which degassed c. 95 % of the total ^{39}Ar released (Fig. 11j). The Ca/K and Cl/K ratios show low contaminations which may be due to some chlorite overgrowth (Supplementary File 4). The plateau consists of the heating steps 5 to 15 which were accessed at 700-1120°C and contain the highest radiogenic argon contents in the York plot (Supplementary File 4). Steps 5 to 12 show some mixing in the $\log_{10}(r/r_0)$ and Arrhenius plots (Fig. 11k, l). The last three steps of the plateau form a domain which is related to rapid cooling through temperatures of c. 476°C (Fig. 11l).

8. (U-Th)/He thermochronology

8.1 Apatite and zircon (U-Th)/He analysis

(U-Th)/He analysis was carried out on apatites of 16 granitoid samples (I- and S-type) from the Neck and mid Central Sulawesi (Table 1.1). Additionally, zircons were analysed from sample SJH03 (Table 1.2) to extend the cooling path.

Ages obtained from the apatites that have not been excluded from further discussion as indicated previously are Pliocene to Pleistocene and range between 1.7 ± 0.1 Ma and 3.7 ± 0.2 Ma. Their age-elevation relationship is summarised in Fig. 12a. The samples analysed show no significant age variations over the range of elevations covered (c. 20 m to 1200 m above sea level), indicating fast uplift and high erosion rates.

Apatite (U-Th)/He ages of samples from the same elevation profile were combined to calculate regional weighted mean ages (Table 2). The results range from 3.1 ± 0.4 Ma in the central Neck region to 2.0 ± 0.8 Ma in the Kambuno area. The calculated weighted mean ages suggest a younging trend towards the south, however, they show no significant age variations at the ±2σ error level.

The zircons analysed from sample SJH03 reveal Late Miocene (U-Th)/He ages between 6.1 ± 0.4 Ma and 7.2 ± 0.4 Ma (Table 1.2). The cooling path between the apatite-He and the zircon-He ages of sample SJH03 is shown in Fig. 12b. If a linear function is assumed a cooling rate of c. 24°C/Ma is indicated. However, if cooling slows down towards the surface, a slightly higher cooling rate of c. 30°C/Ma is estimated for the interval between ~180°C and ~70°C which decreases to c. 15°C/Ma below that.

8.2 Exhumation rates

8.2.1 Age-elevation diagram

Four granitoid samples were sampled from a profile line across the PMC between Tawaeli and Toboli, with an elevation range from 22 to 675 m above sea level. Sample SJH01 yielded only one age of 2.4 ± 0.4 Ma from a single aliquot which does not fit the trend based on the samples collected from the lowest and highest elevations (SJH03 and SJH11_15) and was excluded from the calculation. The slope of the regression line (Fig. 13) gives an exhumation rate of 0.93 mm/yr (R^2 = 0.997) which is similar to exhumation rates of c. 0.7 to 1 mm/yr reported by Bellier et al. (2006) from the west side of the Palu-Koro Fault.

8.2.2 Mean elevation model

Significant topographic variations can influence the closure isotherms of systems which may not have remained in a 'steady state' during exhumation, especially near very low closure temperatures such as those of the (U-Th)/He system. The very young Pliocene to Pleistocene apatite (U-Th)/He ages acquired in this study as well as the medium to high exhumation rates indicated from age-elevation plots suggest that the isotherms are likely to mimic the topographic variations of mountain peaks and valleys.

A mean elevation model was created using ESRI ArcGIS 10.1. The model is based on the approach described by Brandon et al. (1998) and defines the actual depth of the closure isotherm in relation to the sample location. The closure depth for the apatite (U-Th)/He ages was determined by using the programme AGE2EDOT v2.1 (Brandon et al., 1998; Ehlers et al., 2005). A minimum surface temperature of 10°C and thermal gradient of 20°C/km were used as input parameters. The output indicates a geothermal gradient of 27 to 31°C/km and cooling rates of 17-27°C/Ma which are similar to the cooling rates calculated from the apatite and zircon (U-Th)/He ages for sample SJH03. A corresponding closure depth was determined for each apatite (U-Th)/He age acquired. This closure depth was used to calculate the distance of the isotherm with respect to the sample location.

An exhumation rate was determined for each sample using the calculated distance divided by the weighted mean age of the apatite (U-Th)/He system (95% confidence interval) or the apatite (U-Th)/He age (±2σ error) if a single aliquot yielded an age only. The rates acquired range from 0.66 to 0.93 mm/yr in the Neck region, and similar rates of 0.66 to 1.03 mm/yr were analysed from mid Central Sulawesi (Table 2).

9. Discussion

9.1 Metamorphism of the PMC

Metamorphic rocks were previously interpreted as Mesozoic or older basement rocks (Sukamto, 1973; Sopaheluwakan et al., 1995; Parkinson, 1998; Calvert & Hall, 2003; van Leeuwen & Muhardjo, 2005). Recent U-Pb zircon dating on schists of the PMC showed that some of these rocks have Eocene protoliths, identified from detrital zircons, and are therefore younger than previously thought (Hennig et al., 2016; van Leeuwen et al., 2016). Zircon U-Pb rim ages of 3.6 Ma (Hennig et al., 2016) from gneiss of the southern PMC indicate metamorphism during the Pliocene.

691 The schist samples selected for analysis show a strong foliation which is cut by small shear bands,
692 therefore the ages acquired, c. 5.3 and 4.8 Ma from white mica and biotite in the northern PMC, and
693 c. 2.7 Ma from biotite in the southern PMC, are interpreted to record cooling after the last fabric-
694 forming event in which micas recrystallised. The interbanded amphibolite yielded an age of c. 3.1 Ma
695 and has a fine-grained recrystallised texture, and is interpreted to have been completely reset during
696 Pliocene deformation.
697
698 Both cooling ages of the southern PMC (c. 3.1 and 2.7 Ma) are younger than those obtained from
699 micas of the northern PMC schist (c. 5.3 and 4.8 Ma), and therefore indicate that exhumation may
700 have started earlier in the north and became younger southward.
701
702 The mineral assemblage of quartz, feldspar, biotite, andalusite and cordierite identified for sample
703 SJH11_16 suggests relative high temperatures and low pressures. Schists from the area of SJH11_16
704 have almost identical mineral assemblages but some contain staurolite. Multiple thin sections of one
705 hand specimen (SJH32) show that staurolite is very localised because some contain staurolite while
706 others do not. Sample PMC06 is a similar strongly deformed andalusite-cordierite schist but contains
707 small staurolite crystals which are in contact with andalusite, indicating they formed a stable mineral
708 assemblage at low to medium pressures.
709
710 Subordinate garnet was observed in two schist samples from the north (PMC09) and south
711 (SJH11_1214) of the PMC. PMC09 contains andalusite, cordierite and garnet, whereas SJH11_1214
712 lacks andalusite and cordierite. Garnet is suggested to be as localised as staurolite in small volumes
713 of the schists. The garnets have Mn-rich almandine compositions, supporting a high temperature
714 metamorphism. Titanium-in-biotite thermometry was carried out for sample SJH11_1214. Biotite
715 inclusions in garnet are assumed to be in equilibrium with the garnet and record temperatures of
716 622 ± 24°C. Biotite of the dominant foliation yielded similar to slightly higher temperatures of 656
717 and 669 ± 24°C. The Ti-in-biotite for sample PMC09 thermometer yielded similar temperatures from
718 554 to 615 ± 24°C.
719
720 This study suggests that biotite, white mica, andalusite, cordierite, staurolite and Mn-rich garnet
721 observed in the PMC schists form a Buchan-type metamorphic mineral assemblage, opposing former
722 interpretations of an earlier medium-pressure metamorphism with the formation of staurolite and
723 kyanite followed by a high-temperature contact metamorphism containing andalusite and sillimanite
724 (Egeler, 1947). High temperature/low pressure Buchan metamorphism has been described from the

type locality of the Grampian Terrane in NW Scotland, UK (e.g. Ganguly, 1972; Hudson, 1980, 1985). Reported mineral assemblages include andalusite-cordierite-biotite in the andalusite zone, and andalusite-staurolite-cordierite-biotite ± Mn-rich garnets in the staurolite zone (Hudson, 1980).

9.1.1 Inferred cooling and exhumation rates

Several geochronometers were combined to interpret the cooling path of the metamorphic rocks from the southern PMC to the north and west of Toboli. The cooling curve combines zircon U-Pb rim ages of c. 3.6 Ma from biotite (- amphibole) gneiss (Hennig et al., 2016) with $^{40}Ar/^{39}Ar$ cooling ages of amphibole and biotite from nearby amphibolite and biotite schist (Fig. 14).

There is uncertainty in the high temperature part of the cooling path because the zircon crystallisation temperature is unknown. A relatively low temperature of 700°C was chosen to avoid overestimating cooling rates. If closure temperatures indicated by the Arrhenius plots are considered for the medium temperature cooling path reconstruction, an average cooling rate of c. 320 +105/-80°C/Ma is estimated from 700 to 404°C (Fig. 14), which is supported by the biotite and amphibole data (c. 470 +390/-150 °C/Ma). Such rapid cooling implies fast exhumation.

Mylonitic fabrics of the schists indicate the rocks were formed in the mid to lower continental crust (>10 km depth). Mineral assemblages observed indicate relatively high temperatures (c. 500-600 °C) and low to medium pressures (c. 4.0-5.5 kbar). This suggests exhumation from c. 10 to 14 km depth which would require very high exhumation rates of 3-4 mm/yr since the rocks were formed in the mid Pliocene (c. 3.6 Ma). High temperatures and intense deformation, including shear fabrics, indicate extreme stretching and thinning of the crust.

9.2 Cooling histories of magmatic rocks

Granitoid rocks that have intruded the metamorphic rocks must have been emplaced in them prior to exhumation and thus can help to date and characterise the final stage of exhumation. A combination of several geochronometers constrains the cooling and exhumation histories of the granitoid rocks (Fig. 14).

9.2.1 Closure temperature estimates

In this study there was continuous radiogenic Ar release from medium to high temperatures (c. 600 to 1000°C) and only minor mixing with atmospheric argon in the first few steps of the spectrum. The later steps have the highest radiogenic argon release and similar diffusion radii, possibly suggesting

759 no structural changes in the biotite up to ~1000°C. The $\log_{10}(r/r_0)$ and Arrhenius data (Figs. 10 and
760 11) were used to identify domains which show no mixing with either the initial heating steps related
761 to high atmospheric argon contents or the final steps which are often related to excess argon or
762 argon loss due to disintegration as illustrated by the York plot (Supplementary File 4). The domains
763 often include higher temperature steps and were used to determine closure temperature estimates
764 for metamorphic and magmatic biotite. Closure temperatures for metamorphic biotites (c. 380-
765 400°C) are within the commonly accepted estimates of c. 280-400°C (e.g. Harrison et al., 1985;
766 Grove & Harrison, 1996). Magmatic biotites yielded much higher closure temperatures of c. 460-
767 480°C which are higher than commonly accepted estimates.
768
769 The apparent high closure temperatures may be due to structural changes at temperatures of 600°C
770 to 800°C or compositional variations (e.g. Gaber et al., 1988; Lee, 1993) which cannot be ruled out
771 without spectroscopic evidence. Equally, argon diffusivity has been reported to depend on various
772 parameters, such as composition or the cooling rate (Harrison et al., 1985), and could also reflect
773 retentive reservoirs rather than grain modification or decomposition. The existence of possible
774 highly retentive core domains has been demonstrated for K-feldspar of the Capoas Granite in
775 Palawan (Forster et al., 2015), however, these were applied to a non-hydrous mineral, whereas
776 biotites used in this study are thought to be more complex with higher uncertainties.
777
778 Microprobe chemical analyses of biotites from the west Central Sulawesi granitoids indicate they are
779 normal Fe-Mg biotites with no unusual compositions. However, fluorine and barium are present in
780 all four biotite samples. These elements have small ionic radii and indicate relatively narrow
781 interlayers of the crystal lattice which are more difficult to degas compared to wider interlayers
782 containing elements with large ionic radii (Dahl, 1996). They may contribute to the retentivity and
783 high closure temperatures of the biotites.
784
785 Studies of cooling rates by Harrison (1981) and Harrison et al. (1985) showed variations in biotite
786 closure temperatures between 280°C for a low cooling rate of 1°C/Ma and 345°C for a high cooling
787 rate of 100°C/Ma. Reiners & Brandon (2006) demonstrated a similar change in biotite closure
788 temperatures between c. 280°C and c. 380°C for the same range of cooling rates based on the
789 Dodson equation. The cooling rate estimates calculated for the metamorphic and magmatic rocks of
790 west Central Sulawesi exceed the maximum cooling rate of 100°C/Ma used in the previous studies.
791 This may provide an explanation for the enhanced biotite retentivity, resulting in very high closure
792 temperatures.

In summary, although there is some uncertainty on the closure temperature estimates presented here, they yield similar values of c. 380-400°C for biotite of the metamorphic rocks and c. 460-480°C for biotites of the magmatic rocks, thus providing a general indication of the approximate closure temperatures of biotite somewhere between c. 350 and 500°C. An exact quantification is not possible due to the overall assumptions of the numeric model, however, the cooling paths summarised in Fig. 14 are very steep at high to medium temperatures with internally consistent values of the different systems. Therefore, the uncertainties included in the cooling paths are much smaller than the difference between the closure temperature values of the biotites which include the uncertainties of the model. This is illustrated by similar cooling rates that would be obtained if lower closure temperatures were accepted for the biotites (Fig. 14).

9.2.2 I-type magmatic rocks

$^{40}Ar/^{39}Ar$ dating of biotites from I-type magmatic rocks SJH03 and SJH08 yielded Late Miocene cooling ages of 7.2 ± 0.1 Ma and 6.4 ± 0.1 Ma respectively. Sample SJH03 has a crystallisation age of 7.0 ± 0.1 Ma from U-Pb zircon dating (Hennig et al., 2016) which is identical within error to the $^{40}Ar/^{39}Ar$ age. Sample SJH08 has a slightly older crystallisation age of 6.7 ± 0.1 Ma determined from zircon U-Pb geochronology (Hennig et al., 2016).

Identical ages within error as determined for sample SJH03 are possible if cooling rates were as high as 2000°C/Ma initially (Fig. 14), since a decrease in temperature of approximately 150-250°C would then require an elapsed time of only 50-100 ka, which is within the range of uncertainty of these age estimates.

Although the rock has cooled at very high cooling rates in the order of 1500-2000°C/Ma it shows a granitic texture and not a porphyritic hypabyssal texture previously suggested to indicate very rapid cooling rates for plutons larger than c. 5 km in diameter or deeper than an intrusion depth of c. 3 km (Nabelek et al., 2012). Forster et al. (2015) described similar rapid initial cooling rates for the Capoas Granite on Palawan in the Philippines of 1400°C/Ma and interpreted it to be a 7 km-diameter granite stock that was mechanically forced upwards in order to explain the very high cooling rates. However, excellent road cut exposures show the granodiorite SJH03 is demonstrably not a stock. It is also cross-cut by some small dykes which indicate that the rock crystallised at upper crustal levels. We suggest that magma was emplaced at a shallow depth of possibly 2-7 km into cool country rocks. The contact aureoles and/or chilled margins of the pluton insulated the hot magma, giving it enough

time to crystallise and form large crystals. A time interval of c. 50-100 ka is interpreted to be sufficient to produce equigranular phaneritic textures as observed for the granodiorite SJH03.

I-type rocks formed prior to the PMC exhumation. Their tectonic setting is still poorly understood. P-T estimates from I-type rocks in the Neck and west of Palu valley suggest emplacement depths of c. 3-7 km. The cooling curve shows a break in the slope at the zircon (U-Th)/He closure temperature of c. 180°C at which cooling decreased to a much slower rate of c. 30 +14/-8 °C/Ma (Fig. 14). Assuming an elevated geothermal gradient of 30°C/km for the upper kilometres of continental crust, this closure temperature corresponds to an emplacement depth of c. 6 km. Therefore, the break in the slope is suggested to mark the change from crystallisation to exhumation, with a maximum exhumation rate of c. 0.9 mm/yr. This rate is similar to rates determined from apatite (U-Th)/He analysis across west Central Sulawesi for the uppermost 2 km of continental crust (0.7-1 mm/yr), indicating exhumation from shallow emplacement depth as the product of high erosion rates in a tectonically active tropical region.

9.2.3 S-type granitoids

Biotite $^{40}Ar/^{39}Ar$ ages of 3.1 ± 0.1 Ma (SJH01) and 3.3 ± 0.1 Ma (SJH30) are similar to zircon U-Pb ages of 3.1 ± 0.2 Ma (SJH01) and 3.1 ± 0.1 Ma from a nearby outcrop (SJH11_107) respectively (Hennig et al., 2016).

$^{40}Ar/^{39}Ar$ and U-Pb ages acquired for sample SJH01 are identical within error (Fig. 14). Like sample SJH03, this indicates cooling rates as high as 2000°C/Ma for a temperature decrease of approximately 150-250°C within c. 50-100 ka which is within the range of uncertainty of these age estimates. The granite is part of a complex system of injected dykes into the metamorphic rocks that were subsequently inflated to voluminous bodies, and show cross-cutting relationships of younger generations of dykes, which supports an interpretation of a melt that crystallised at a mid crustal emplacement level rather than a solid stock being pushed through the crust. The initial cooling rates obtained from SJH01 and SJH03 suggest that it is possible to form granitic textures within a time period of c. 50-100 ka.

The apatite (U-Th)/He age obtained is slightly younger at 2.4 ± 0.4 Ma and results in a decrease of the cooling rate to c. 540 +900/-210 °C/Ma between 460°C and 70°C. This suggests exceptionally rapid cooling through the middle to upper crust. Since the cooling path is steep throughout, it is rather uncertain when the rock was emplaced. An emplacement depth of c. 13 km could be inferred

from the slight decrease in the slope of the cooling path at c. 400°C (Fig. 14) and a geothermal gradient of 30°C/km, thus suggesting similar depths and exhumation rate estimates as the PMC schist host rocks.

9.2.4 Extension-related metamorphism, magmatism and exhumation of the PMC

Comparison of cooling through medium to low temperatures for samples SJH03 and SJH01 reveals very different rates and are in the order of ten times higher for SJH01 than for SJH03 (Fig. 14). Fig. 8 shows a major fault, which is part of the major Palu-Koro strike-slip fault system, that separates upper crustal rocks in the west from mid to lower crustal rocks to the east side, representing the boundary of the PMC.

Cooling and exhumation rates determined from S-type magmatic and metamorphic rocks of the PMC are very high (c. 320-540°C/Ma) and up to several millimetres per year (max. ~4 mm/yr). These are significantly higher rates than those reported for mountain uplift as a consequence solely of erosion at average rates of c. 15°C/Ma and c. 0.1-0.5 mm/yr (Brandon et al., 1998; Reiners & Brandon, 2006), as well as determined in this study for I-type magmatic rocks during exhumation by erosion and normal faulting (0.75-0.9 mm/yr).

Widespread granites intruded the PMC including SJH01 which crystallised at c. 3 Ma, was rapidly exhumed at c. 2 Ma, and similar granites were eroded into sediments of the Celebes Molasse which contains zircons of c. 2-3 Ma (Nugraha, 2016) and unconformably overlie metamorphic rocks of the PMC and the granites of only slightly greater age. This shows extraordinarily fast exhumation.

The PMC was exhumed in the Early Pliocene in the north (c. 5.3 Ma) and mid/Late Pliocene in the south (c. 3.1-2.7 Ma). The ages are very similar to magmatic zircon U-Pb ages of S-type granitoids at c. 5 Ma to 2.5 Ma (Hennig et al., 2016) and apatite (U-Th)/He ages of c. 3.7-1.7 Ma, indicating that crystallisation of the S-type magmatic rocks occurred during exhumation.

Contemporaneous metamorphism and magmatism are interpreted as the result of extension. This contradicts previously suggested compressional models, including thrusting at c. 5 Ma from the collision of the Banggai-Sula micro-continental block (e.g. Smith & Silver, 1991; Bergman et al., 1996; Hall, 1996; Maulana et al., 2013). A compressional setting would need to involve considerable crustal thickening over a longer period of time in order to produce high-grade metamorphic rocks and cause anatectic melting. Therefore, an extensional setting is favoured as this would explain the high

temperature/ low pressure mineral assemblages observed in the schists, formation of shear zones as well as simultaneous metamorphism and magmatism caused by a high heat flow due to upwelling of the asthenosphere as a consequence of stretching and thinning of the crust which results in thermal weakening of the crust and decompressional melting (e.g. Lister et al., 1986; Viete et al., 2010). The presence of staurolite alongside andalusite, cordierite and Mn-rich garnet supports a regional Buchan-type metamorphism at high temperature/ low pressure conditions which is consistent with isobaric or decompressional heating in an extensional setting. Much higher pressures would be expected if these rocks were formed by burial under compression.

Field observations including SC shear fabrics and mylonitic shear bands, quartz boudins at centimetre-scale and boudinage of granitic dykes at metre-scale, as well as low-angle normal faults with locally detached schist fragments indicate the PMC was exhumed in an extensional setting. Furthermore, the cooling and exhumation history of the metamorphic rocks and intruded magmatic rocks presented in this study indicate that these mid to lower crustal rocks were brought to the surface very rapidly, a feature consistent with a metamorphic core complex, as proposed by van Leeuwen & Muhardjo (2005) and van Leeuwen et al. (2016). However, a main detachment fault has not been identified. This may be due to intense rainforest vegetation and inaccessibility of the complex, or the PMC may differ from a classical metamorphic core complex. Mylonitic shear zones observed in biotite hornfels and slate north of the PMC may be related to subordinate detachment faults (Fig. 2b).

Thinned crust results in elevated and compressed isotherms that are crossed in a relatively short time during cooling which would explain similar ages recorded by different geochronometers, e.g. identical zircon U-Pb and biotite $^{40}Ar/^{39}Ar$ ages, as well as similar apatite (U-Th)/He ages. Rapid exhumation was accompanied by decompression. This was enhanced by melting which produced abundant granitoid rocks and migmatite found in association with high-grade gneiss and granulite to the south of the PMC which decrease the average density of the lower crust and weaken the rheology (e.g. Lister & Davis, 1989).

Notably, the cooling and exhumation rates estimated in this study significantly exceed the cooling rates for continental core complex exhumation reported in the literature of >50°C/Ma during rapid exhumation, followed by slower cooling at <20°C/Ma (Whitney et al., 2013). For example, crystalline basement rocks of the Rechnitz metamorphic core complex and associated sedimentary hanging wall rocks in the Eastern Alps indicate maximum cooling rates of c. 40-50°C/Ma and exhumation

929 rates of 2 mm/yr during Middle Miocene extension (Dunkl & Demény, 1997; Dunkl et al., 1998), and
930 cooling and exhumation rates of the Eocene to Oligocene Chapedony metamorphic core complex of
931 the Iranian plateau were reported at c. 45-80°C/Ma and 0.75-1.3 mm/yr, respectively
932 (Kargaranbafghi & Neubauer, 2015). In contrast, the Menderes core complex in western Anatolia
933 gives comparable elevated cooling rates of c. 60-120°C/Ma and exhumation rates of c. 1.8-3.3
934 mm/yr during a Pliocene to Pleistocene phase of exhumation (Baran et al., 2017). This poses the
935 question if the rates obtained from the PMC are unique to this area or if the PMC can provide
936 further insights into the actual rates and kinematics of metamorphic complex exhumation due to its
937 very young, Pliocene age.
938
939 Rapid uplift of the PMC has been accompanied by rapid subsidence in Gorontalo Bay as identified by
940 mid Pliocene carbonates which are adjacent to the complex and drowned to c. 800-900 m depth
941 (Fig. 8), as well as minor deposits of clastic sediments which were deposited during the Late Miocene
942 and are now overturned in places (Nugraha, 2016). An interplay between exhumation and
943 subsidence has been proposed for this area where the rebound and exhumation of the crust, driven
944 by extension and decompression, affects the hot and weak lower crustal rocks, triggering its flow
945 towards the root zone of elevated areas in decompressed sites (Hall, 2011). As a result these are
946 bowed upwards while adjacent areas must subside, providing further accommodation space for
947 reworked sediments which in turn increase the load on the weak lower crustal rocks in the basin and
948 cause elevated areas further to rise (Hall, 2011). In that process the metamorphic complex is further
949 metamorphosed during exhumation as evidenced by abundant shear zones and prograde heating
950 with the formation of biotite, white mica and sillimanite in shear planes.
951
952 Late-stage exhumation of the complex was controlled by brittle faults. Minor brittle faults within the
953 PMC dip to the north at low angles and indicate a north-directed movement which is probably the
954 result of extension. The complex is bounded by the transtensional NW-trending Palu-Koro Fault to
955 the west and the Tambarana Fault to the east (Pholbud et al., 2012). They are interpreted to
956 represent the main faults which have facilitated northward stretching of the Neck and possibly also
957 enabled rapid exhumation. Frankel et al. (2015) demonstrated the contribution of normal faults
958 along the Black Mountain fault zone to deformation and extension within the Basin and Range
959 province and proposed dip-slip rates of 1.2 +0.3/-0.2 mm/yr and 1.6 +0.6/-0.4 mm/yr. Several minor
960 sub-parallel NNE-SSW to NE-SW-oriented strike-slip faults were observed within the PMC.
961

962 The mechanism for extension in Western Sulawesi and formation of the PMC is still poorly
963 understood but northward subduction rollback at the North Sulawesi Trench, resulting in clockwise
964 rotation of the North Arm (e.g. Surmont et al., 1994), is very likely an important mechanism from the
965 Pliocene (~3 Ma).
966
967 The PMC seems to have recorded rapid episodic pulses of exhumation rather than a steady-state
968 continuous exhumation at moderate rates. This could imply that older metamorphic core complexes,
969 from which much lower cooling and exhumation rates have been reported, may have been exhumed
970 in a similar way but rates appear lower because they were averaged over longer periods of time.
971
972 Extension is widespread in eastern Indonesia during the Neogene (e.g. Hinschberger et al., 2005;
973 Spakman & Hall, 2010; Hall, 2011, 2012; Pownall et al., 2014), resulting in equally rapid cooling and
974 exhumation reported for example in Seram (Pownall, 2015; Pownall et al., 2014, 2017). Sulawesi,
975 and other parts of eastern Indonesia, offer a unique opportunity to study the mechanisms,
976 exhumation histories and exhumation rates in very young orogens.
977

978 ## 10. Conclusions

979 (1) $^{40}Ar/^{39}Ar$ ages from white mica, biotite and amphibole from schists and interbanded
980 recrystallised amphibolites reveal cooling below ~570-370 °C during the Early Pliocene (c. 5.3 - 4.8
981 Ma) in the north, and Late Pliocene (c. 3.1 - 2.7 Ma) in the south.
982
983 (2) Cooling of these metamorphic minerals during Pliocene metamorphism is also recorded in zircon
984 rims (c. 3.6 Ma) of gneisses to the east near Toboli, and in combination with $^{40}Ar/^{39}Ar$ ages, reveal
985 high cooling rates of c. 320 +105/-80 °C/Ma for the PMC.
986
987 (3) The metamorphic rocks of the PMC are intruded by an S-type granitoid, which has a mid Pliocene
988 zircon U-Pb crystallisation age of c. 3.1 Ma (Hennig et al., 2016), indicating that magmatism was
989 contemporaneous with metamorphism. $^{40}Ar/^{39}Ar$ and (U-Th)/He ages from the granitoid are very
990 similar ($^{40}Ar/^{39}Ar$: ~3.1 Ma) to slightly younger ((U-Th)/He: ~2.4 Ma), supporting rapid cooling and
991 exhumation of the granitoid and metamorphic host rocks.
992
993 (4) These rocks were exhumed from at least 2 km depth, and reworked into the Plio- to Pleistocene
994 Celebes Molasse which unconformably overlies the metamorphic rocks (van Leeuwen & Muhardjo,
995 2005; Nugraha, 2016).

(5) This requires high exhumation rates of up to several millimetres per year. Estimates from the PMC metapelites suggest exhumation from possible depths of c. 10-14 km, resulting in estimated exhumation rates of c. 3-4 mm/yr.

(6) Pliocene magmatism (c. 3.1 Ma) was contemporaneous with metamorphism and rapid exhumation of the PMC which is interpreted as a result of decompressional melting from stretching and thinning of the crust in an extensional setting.

(7) Late Miocene I-type magmatic intrusions expose higher crustal levels which are separated from the PMC by strands of the Palu-Koro Fault. These rocks west of the PMC show moderate rates of cooling (~30°C/Ma) and exhumation (c. 0.75-0.9 mm/yr) after emplacement for a time interval between c. 6.7 and 2.9 Ma, probably related to normal faulting and increased erosion in tropical environments.

(8) Results of this study show that formation of magmatic rocks, exhumation, and reworking into a sediment can occur within ~1 Ma. Cooling and exhumation rates estimated in this study record very young exhumation and significantly exceed the cooling rates for most continental core complex exhumation reported in the literature, which are interpreted to be apparent rates averaged over significantly longer periods.

Acknowledgements

This study was supported by the SE Asia Research Group which is funded by a consortium of oil companies. We thank Afif Saputra and Alfend Rudyawan for their help and assistance during fieldwork, as well as Mike Cottam, Ian Watkinson and Tim Breitfeld for helpful discussions. $^{40}Ar/^{39}Ar$ analysis was undertaken at ANU RSES Argon Facility. We also thank Abaz Alimanovic who performed the (U-Th)/He analysis, Andrew Beard for assisting with the mineral chemical analysis (EDS/WDS-SEM), and Yuntao Tian for assistance in creating the mean elevation model. The University of Melbourne thermochronology laboratory receives infrastructure support under the National Collaborative Research Infrastructure Strategy AuScope program. Further, we thank Fred Jourdan and two anonymous reviewers for their thorough comments which greatly improved the manuscript.

References

Abdel-Rahman, A.F.M., 1994. Nature of biotites from alkaline, calc-alkaline and peraluminous magmas. Journal of Petrology 35, 525-541.

Ahlburg, J., 1913. Versuch einer geologischen Darstellung der Insel Celebes. Neue Folge Band 12, 172 pp.

Anderson, J.L., Smith, D.R., 1995. The effects of temperature and fO2 on the Al-in-hornblende barometer. American Mineralogist 8, 549–559.

Apandi, T., 1977. Geologic map of the Kotamobagu Quadrangle, North Sulawesi – scale 1: 250,000. Geological Survey of Indonesia, Directorate of Mineral Resources, Geological Research and Development Centre, Bandung.

Bachri, S., Sukido, Ratman, N., 1993. Geology of the Tilamuta Sheet, Sulawesi – scale 1: 250,000. Geological Survey of Indonesia, Directorate of Mineral Resources, Geological Research and Development Centre, Bandung.

Baran, Z.O., Dilek, Y., Stockli, D., 2017. Diachronous uplift and cooling history of the Menderes core complex, western Anatolia (Turkey), based on new Zircon (U-Th)/He ages. Tectonophysics 694, 181-196.

Bellier, O., Sebrier, M., Seward, D., Beaudouin, T., Villeneuve, M., Putranto, E., 2006. Fission track and fault kinematics analyses for new insight into the Late Cenozoic tectonic regime changes in West-Central Sulawesi (Indonesia). Tectonophysics 413, 3-4, 201-220.

Beltrando, M., Lister, G.S., Forster, M.A., Dunlap, W.J., Fraser, G., Hermann, J., 2009. Dating microstructures by the Ar-40/Ar-39 step-heating technique: deformation-pressure-temperature-time history of the Penninic Units of the Western Alps. Lithos 113, 801-819.

Bergman, S.C., Coffield, D.Q., Talbot, J.P., Garrard, R.J., 1996. Tertiary tectonic and magmatic evolution of Western Sulawesi and the Makassar Strait, Indonesia: evidence for a Miocene collision, In: Hall, R., Blundell, D.J (Eds), Tectonic Evolution of SE Asia. Geological Society of London Special Publication 106, 391 -430.

Brandon, M.T., Roden-Tice, M.K., Garver, J.I., 1998. Late Cenozoic exhumation of the Cascadia accretionary wedge in the Olympic Mountains, Northwest Washington State. Geological Society of America Bulletin 110, 985–1009.

Brouwer, H.A., 1934. Geologische onderzoekingen op het eiland Celebes. Verhandelingen Koninklijk Nederlands Geologisch en Mijnbouwkundig Genootschap, Geologische Serie V, 10, 39-218.

Brown, R.W., Beucher, R., Roper, S., Persano, C., Stuart, F., Fitzgerald. P., 2013. Natural age dispersion arising from the analysis of broken crystals. Part I: Theoretical basis and implications for the apatite (U–Th)/He thermochronometer. Geochimica et Cosmochimica Acta 122, 478-497.

Calvert, S.J., Hall, R., 2003. The Cenozoic geology of the Lariang and Karama regions, Western Sulawesi: New insight into the evolution of the Makassar Straits region. Proceedings Indonesian Petroleum Association, 29th Annual Convention 2003, 501–517.

Calvert, S.J., Hall, R., 2007. Cenozoic Evolution of the Lariang and Karama regions, North Makassar Basin, western Sulawesi, Indonesia. Petroleum Geoscience 13, 353-368.

Camplin, D.J., Hall, R., 2014. Neogene history of Bone Gulf, Sulawesi, Indonesia. Marine and Petroleum Geology 57, 88-108.

Cottam, M.A., Hall, R., Forster, M.A., Boudagher-Fadel, M.K., 2011. Basement character and basin formation in Gorontalo Bay, Sulawesi, Indonesia: new observations from the Togian Islands. In: Hall, R., Cottam, M.A., Wilson, M.E.J. (Eds.), The SE Asian Gateway: History and Tectonics of the Australia-Asia collision. Geological Society of London Special Publication 355, 177-202.

Dahl, P.S., 1996. The crystal-chemical basis for argon retention in micas: inferences from interlayer partitioning and implications for geochronology. Contributions to Mineralogy and Petrology 123, 22-39.

Deer, W.A., Howie, R.A., Zussman, J., 1962. Rock-forming Minerals. Sheet Silicates. Longmans, London.

Dodson, M.H., 1973. Closure temperatures in cooling geological and petrological systems. Contribution to Mineralogy and Petrology 40, 259-274.

Dunkl, I., Demény, A., 1997. Exhumation of the Rechnitz Window at the border of the Eastern Alps and Pannonian Basin during Neogene extension. Tectonophysics 272(2), pp.197-211.

Dunkl, I., Grasemann, B., Frisch, W., 1998. Thermal effects of exhumation of a metamorphic core complex on hanging wall syn-rift sediments: an example from the Rechnitz Window, Eastern Alps. Tectonophysics 297(1), 31-50.

Egeler, C.G., 1947. Contribution to the petrology of the metamorphic rocks of western Celebes. Geological Expedition to the Island of Celebes, University of Amsterdam, 185-346.

Ehlers, T.A., Farley, K.A., 2003. Apatite (U–Th)/He thermochronometry: methods and applications to problems in tectonics and surface processes. Earth Planetary Science Letters 206, 1–14.

Ehlers, T.A., Chaudhri, T., Kumar, S., Fuller, C.W., Willett, S.D., Ketcham, R.A., Brandon, M.T., Belton, D.X., Kohn, B.P., Gleadow, A.J.W., Dunai, T.J., Fu, F.Q., 2005. Computational tools for low-temperature thermochronometer interpretation. Reviews in Mineralogy and Geochemistry 58, 589–622.

Elburg, M., van Leeuwen, T., Foden, J., Muhardjo, 2003. Spatial and temporal isotopic domains of contrasting igneous suites in Western and Northern Sulawesi, Indonesia. Chemical Geology 199, 3-4, 243-276.

Farley, K.A., Wolf, R.A., Silver, L.T., 1996. The effects of long alpha-stopping distances on (U-Th)/He ages. Geochimica et Cosmochimica Acta 60, 4223–4229.

Farley, K.A., 2000. Helium diffusion from apatite: general behaviour as illustrated by Durango fluorapatite. Journal of Geophysical Research 105, 2903-2914.

Fitzgerald, P.G., Baldwin, S.L., Webb, L.E., O'Sullivan, P.B., 2006. Interpretation of (U–Th)/He single grain ages from slowly cooled crustal terranes: A case study from the Transantarctic Mountains of southern Victoria Land. Chemical Geology 225, 91-120.

Forster, M.A., Lister, G.S., 2004. The interpretation of $^{40}Ar/^{39}Ar$ apparent age spectra produced by mixing: Application of the method of asymptotes and limits. Journal of Structural Geology 26, 287–305.

Forster, M.A., Lister, G.S., 2010. Argon enters the retentive zone: reassessment of diffusion parameters for K-feldspar in the South Cyclades Shear Zone, Ios, Greece. Geological Society of London Special Publications 332, 17-34.

Forster, M. A., Lister, G. S., 2014. $^{40}Ar/^{39}Ar$ geochronology and the diffusion of ^{39}Ar in phengite-muscovite intergrowths during step-heating experiments *in vacuo*. Geological Society of London Special Publication 378, 117-135.

Forster, M. A., Armstrong, R., Kohn, B., Lister, G.S., Cottam, M.A., Suggate, S., 2015. Highly retentive core domains in K-feldspar and their implications for $^{40}Ar/^{39}Ar$ thermochronology illustrated by determining the cooling curve for the Capoas Granite, Palawan, The Philippines. Australian Journal of Earth Sciences 62, 883-902.

Frankel, K.L., Owen, L.A., Dolan, J.F., Knott, J.R., Lifton, Z.M., Finkel, R.C., Wasklewicz, T., 2015. Timing and rates of Holocene normal faulting along the Black Mountains fault zone, Death Valley, USA. Lithosphere 8, 3-22.

Gaber, L.J., Foland, K.A., Corbató, C.E., 1988. On the significance of argon release from biotite and amphibole during $^{40}Ar/^{39}Ar$ vacuum heating. Geochimica et Cosmochimica Acta 52, 2457-2465.

Ganguly, J., 1972. Staurolite stability and related parageneses: theory, experiments and applications. Journal of Petrology 13, 335-36.

Gleadow, A., Harrison, M., Kohn, B., Lugo-Zazueta, R., Phillips, D., 2015. The Fish Canyon Tuff: A new look at an old low-temperature thermochronology standard. Earth and Planetary Science Letters 424, 95-108.

Grove, M., Harrison, T.M., 1996. $^{40}Ar^*$ diffusion in Fe-rich biotite. American Mineralogist 81, 940-951.

Guntoro, A. 1999. The formation of the Makassar Strait and the separation between SE Kalimantan and SW Sulawesi. Journal of Asian Earth Sciences 17, 79–98.

Hall, R., 1996. Reconstructing Cenozoic SE Asia. In: Hall, R., Blundell, D.J. (Eds.), Tectonic Evolution of SE Asia. Geological Society of London Special Publication 106, 153-184.

Hall, R., 2011. Australia-SE Asia collision: plate tectonics and crustal flow. In: Hall, R., Cottam, M.A., Wilson, M.E.J. (Eds.), The SE Asian Gateway: History and Tectonics of the Australia-Asia collision. Geological Society of London Special Publication 355, 75-109.

Hall, R., 2012. Late Jurassic-Cenozoic reconstructions of the Indonesian region and the Indian Ocean. Tectonophysics 570-571, 1-41.

Hall, R., Clements, B., Smyth, H.R., 2009. Sundaland: basement character, structure and plate tectonic development. Proceedings Indonesian Petroleum Association, 33rd Annual Convention. IPA09-G-134.

Hall, R., Wilson, M.E.J., 2000. Neogene sutures in eastern Indonesia. Journal of Asian Earth Sciences 18, 787-814.

Hall, R., Sevastjanova, I., 2012. Australian crust in Indonesia. Australian Journal of Earth Sciences 59, 827-844.

Hamilton, W., 1979. Tectonics of the Indonesian region. U. S. Geological Survey Professional Paper 1078, 345 pp.

Harrison, T.M., 1981. Diffusion of ^{40}Ar in hornblende. Contributions of Mineralogy and Petrology 78, 324-331.

Harrison, T.M., Duncan, I., McDougall, I., 1985. Diffusion of ^{40}Ar in biotite: temperature, pressure and compositional effects. Geochimica et Cosmochimica Acta 49, 2461-2468.

Harrison, T.M., Grove, M., Lovera, O.M., Zeitler, P.K., 2005. Continuous thermal histories from closure profiles. Reviews in Mineralogy and Geochemistry 58, 389-409.

Hennig, J., Advokaat, E., Rudyawan, A., Hall, R., 2014. Large sediment accumulations and major subsidence offshore; rapid uplift on land: consequences of extension of Gorontalo Bay and northern Sulawesi. Proceedings Indonesian Petroleum Association, 38th Annual Convention and Exhibition, IPA14-G-304.

Hennig, J., Hall, R., Armstrong, R.A., 2016. U-Pb zircon geochronology of rocks from west Central Sulawesi, Indonesia: Extension-related metamorphism and magmatism during the early stages of mountain building. Gondwana Research 32, 41-63.

Henry, D.J., Guidotti, C.V., Thomson, J.A., 2005. The Ti-saturation surface for low-to-medium pressure metapelitic biotites: Implications for geothermometry and Ti-substitution mechanisms. American Mineralogist 90, 316-328.

Hinschberger, F., Malod, J.-A., Réhault, J.-P., Villeneuve, M., Royer, J.-Y., Burhanuddin, S., 2005. Late Cenozoic geodynamic evolution of eastern Indonesia. Tectonophysics 404, 91-118.

Holland, T.J.B., Blundy, J.D., 1994. Non-ideal interactions in calcic amphiboles and their bearing on amphibole-plagioclase thermometry. Contributions to Mineralogy and Petrology 116, 433-447.

Hudson, N.F.C., 1980. Regional metamorphism of some Dalradian pelites in the Buchan area, NE Scotland. Contributions to Mineralogy and Petrology 73, 39-51.

Hudson, N.F.C., 1985. Conditions of Dalradian metamorphism in the Buchan area, NE Scotland. Journal of the Geological Society 142, 63-76.

Jablonski, D., Priyono, R., Westlake, S., Larsen, O.A., 2007. Geology and exploration potential of the Gorontalo Basin, Central Indonesia - eastern extension of the North Makassar Basin? Indonesian Petroleum Association, Proceedings 31st Annual Convention, 197-224.

1230 Kargaranbafghi, F., Neubauer, F., 2015. Lithospheric thinning associated with formation of a
1231 metamorphic core complex and subsequent formation of the Iranian plateau. GSA Today 25(7), 4-8.
1232
1233 Kavalieris, I., van Leeuwen, T.M., Wilson, M., 1992. Geological setting and styles of mineralization,
1234 North Arm of Sulawesi, Indonesia. Journal of Southeast Asian Earth Sciences 7, 113-129.
1235
1236 Lee, J.K.W., 1993. The argon release mechanisms of hornblende in vacuo. Chemical Geology (Isotope
1237 Geoscience Section) 106, 133-170.
1238
1239 Lister, G.S., Davis, G.A., 1989. The origin of metamorphic core complexes and detachment faults
1240 formed during Tertiary continental extension in the northern Colorado River region, U.S.A. Journal of
1241 Structural Geology 11, 65-94.

1242 Lister, G.S., Etheridge, M.A., Symonds, P.A., 1986. Detachment faulting and the evolution of passive
1243 continental margins. Geology 14, 246-250.

1244 Lovera, O.M., Richter, F.M., Harrison, T.M., 1989. The $^{40}Ar/^{39}Ar$ thermochronometry for slowly
1245 cooled samples having a distribution of diffusion domain sizes. Journal of Geophysical Research 94,
1246 17,917–17,935.
1247
1248 Lovera, O.M., Richter, F.M., Harrison, T.M., 1991. Diffusion domains determined by ^{39}Ar released
1249 during step heating. Journal of Geophysical Research 96, 2057-2069.
1250
1251 Ludwig, K.R., 2003. User's Manual for Isoplot 3.0: A Geochronological Toolkit for Microsoft Excel.
1252 Berkeley Geochronology Center Special Publication 4, 71 pp.
1253
1254 Maulana, A., Watanabe, K., Imai, A., Yonezu, K., 2013. Petrochemical characteristic and
1255 geothermobarometry study of the granitic rocks from Sulawesi, Indonesia: Implications on
1256 exhumation and tectonomagmatic process. Journal of Earth System Science, (in press).
1257
1258 McDowell, F.W., McIntosh, W.C., Farley, K.A., 2005. A precise $^{40}Ar/^{39}Ar$ reference age for the
1259 Durango apatite (U–Th)/He and fission-track dating standard. Chemical Geology 214, 249-263.
1260
1261 Metcalfe, I., 2009. Late Palaeozoic and Mesozoic tectonic and palaeogeographical evolution of SE
1262 Asia. In: Buffetaut, E., Cuny, G., Le Loeuff, J., Suteethorn, V. (Eds.), Late Palaeozoic and Mesozoic
1263 Ecosystems in SE Asia. Geological Society of London Special Publication 315, 7-23.
1264
1265 Nabelek, P.I., Hofmeister, A.M., Whittington, A. G., 2012. The influence of temperature-dependent
1266 thermal diffusivity on the conductive cooling rates of plutons and temperature-time paths in contact
1267 aureoles. Earth and Planetary Science Letters 317-318, 157-164.
1268
1269 Nugraha, A.M.S., 2016. Late Cenozoic history of Sulawesi, Indonesia: The Celebes Molasse. Royal
1270 Holloway University of London, Ph.D. thesis, 424 pp.
1271
1272 Parkinson, C., 1998. An outline of the petrology, structure and age of the Pompangeo Schist Complex
1273 of central Sulawesi, Indonesia. Island Arc 7, 231-245.
1274
1275 Passchier, C.W., Trouw, R.A.J., 2005. Microtectonics, 2nd edition. Springer Verlag, 366 pp.
1276

Pezzati, G., Hall, R., Burgess, P., Perez-Gussinye, M., 2014. Core complex exhumation on land and rapid subsidence in Gorontalo Bay, Sulawesi (Indonesia). American Geophysical Union, Fall Meeting 2014, abstract T43A-4702.

Pholbud, P., Hall, R., Advokaat, E., Burgess, P., Rudyawan, A., 2012. A new interpretation of Gorontalo Bay, Sulawesi. Proceedings, Indonesian Petroleum Association, 36th Annual Convention. IPA12-G-029, 197-224.

Polvé, M., Maury, R.C., Bellon, H., Rangin, C., Priadi, B., Yuwono, S., Joron, J.L., Atmadja, R.S., 1997. Magmatic evolution of Sulawesi (Indonesia): Constraints on the Cenozoic geodynamic history of the Sundaland active margin. Tectonophysics 272, 1, 69-92.

Pownall, J.M., Hall, R., Armstrong, R.A., Forster, M.A., 2014. Earth's youngest known ultrahigh-temperature granulites discovered on Seram, eastern Indonesia. Geology 42, 4, 279-282.

Pownall, J.M., 2015. UHT metamorphism on Seram, eastern Indonesia: reaction microstructures and P-T evolution of spinel-bearing garnet-sillimanite granulites from the Kobipoto Complex. Journal of Metamorphic Geology 33, 909-935.

Pownall, J.M., Forster, M.A., Hall, R., Watkinson, I.M., 2017. Tectonometamorphic evolution of Seram and Ambon, eastern Indonesia: Insights from $^{40}Ar/^{39}Ar$ geochronology. Gondwana Research 44, 35-53.

Priadi, B., Polvé, M., Maury, R.C., Bellon, H., Soeria-Atmadia, R., Joron, J.L., Cotten, J., 1994. Tertiary and Quaternary magmatism in Central Sulawesi: chronological and petrological constraints. Journal of Southeast Asian Earth Sciences 9, 81-93.

Ratman, N., 1976. Geological Map of the Tolitoli Quadrangle, North Sulawesi - 1:250,000, Geological Research and Development Centre, Bandung.

Ratman, N., Atmawinata, S., 1993. Geology of the Mamuju Quadrangle Sulawesi – scale 1:250,000. Geological Research and Development Centre, Bandung.

Reiners, P.W., Spell, T.L., Nicolescu, S., Zanetti, K.A., 2004. Zircon (U–Th)/He thermochronometry: He diffusion and comparisons with $^{40}Ar/^{39}Ar$ dating. Geochimica et Cosmochimica Acta 68, 1857–1887.

Reiners, P.W., Brandon, M.T., 2006. Using Thermochronology to Understand Orogenic Erosion. Annual Reviews of Earth and Planetary Science 34, 419-466.

Rudyawan, A., 2015. Neogene Stratigraphy, Structure and Magmatism of the Central North Arm of Sulawesi, Indonesia. Ph.D. thesis, Royal Holloway University of London, 484 pp.

Sarasin, P., Sarasin, F., 1901. Material zur Naturgeschichte der Insel Celebes: Bd. Entwurf einer geografisch- geologischen Beschreibung der Insel Celebes. Anhang: Untersuchung einiger Gesteinssuiten, gesammelt in Celebes von P. und F. Sarasin, von Schmidt. Vol. 4. CW Kreidel's Verlag, Wiesbaden, Deutschland.

Satyana, A.H., 2015. Rifting history of the Makassar Straits: New constraints from wells penetrating the basement and oils discovered in Eocene section – implications for further exploration of West Sulawesi offshore. Proceedings Indonesian Petroleum Association, 39th Annual Convention and Exhibition, IPA15-G-104.

Shuster, D.L., Flowers, R.M., Farley, K.A., 2006. The influence of natural radiation damage on helium diffusion kinetics in apatite. Earth and Planetary Science Letters 249, 148–161.

Simandjuntak, T.O., Rusmana, E., Surono, Supandjono, J.B., 1991. Geological map of the Malili Quadrangle, Sulawesi – scale 1:250,000. Geological Research and Development Centre, Bandung.

Simandjuntak, T.O., Surono, Supandjono, J.B., 1997. Geological map of the Poso Quadrangle, Sulawesi – 1:250,000. Geological Research and Development Centre, Bandung.

Situmorang, B., 1982. Formation, evolution and hydrocarbon prospects of the Makassar Basin, Indonesia. In: Watson, S.T. (Ed.), Transactions of the 3rd Circum Pacific Energy and Mineral Resources Conference, Honolulu, Hawaii, 227-232.

Smith, R.B., Silver, E.A., 1991. Geology of a Miocene collision complex, Buton, eastern Indonesia. Geological Society of America Bulletin 103, 660-678.

Smyth, H.R., Hamilton, P.J., Hall, R., Kinny, P.D., 2007. The deep crust beneath island arcs: inherited zircons reveal a Gondwana continental fragment beneath East Java, Indonesia. Earth and Planetary Science Letters 258, 269-282.

Socquet, A., Simons, W., Vigny, C., McCaffrey, R., Subarya, C., Sarsito, D., Ambrosius, B., Spakman, W., 2006. Microblock rotations and fault coupling in SE Asia triple junction (Sulawesi, Indonesia) from GPS and earthquake slip vector data. Journal of Geophysical Research: Solid Earth 111 (B8).

Sopaheluwakan, J., Kadarusman, A., Priadi, B., Utoyo, H., 1995. The nature of the basement rocks in the Palu region, Central Sulawesi: The newly found eclogite and its regional implication. Neogene Evolution of Pacific: Biotic. Proceedings of the Sixth International Congress on Pacific Neogene Biostratigraphy and IGCP 355. Oceanographic and Tectonic Development, Kyoto Institute of Natural History, Kyoto, Japan, 73–79.

Spakman, W., Hall, R., 2010. Surface deformation and slab-mantle interaction during Banda arc subduction rollback. Nature Geoscience 3, 562–566.

Spell, T.L., McDougall, I., 2003. Characterization and calibration of Ar-40/Ar-39 dating standards. Chemical Geology 198, 189-211.

Spiegel, C., Kohn, B., Belton, D., Berner, Z., Gleadow, A., 2009. Apatite (U–Th–Sm)/He thermochronology of rapidly cooled samples: The effect of He implantation. Earth and Planetary Science Letters 285, 105-114.

Sukamto, R., 1973. Reconnaissance geologic map of Palu Area, Sulawesi – scale 1:250,000. Geological Research and Development Centre, Bandung.

Sukamto, R., 1975. The structure of Sulawesi in the light of plate tectonics, Regional Conference on the Geology and Mineral Resources of Southeast Asia, 121-141.

Sukido, Sukarna, D., Sutisna, K., 1993. Geological Map of the Pasangkayu Quadrangle, Sulawesi – scale 1:250,000. Geological Research and Development Centre, Bandung.

Surmont, J., Laj, C., Kissal, C., Rangin, C., Bellon, H., Priadi, B., 1994. New paleomagnetic constraints on the Cenozoic tectonic evolution of the North Arm of Sulawesi, Indonesia. Earth and Planetary Science Letters 121, 629-638.

Taylor, S.R., McLennan, S.M., 1997. The origin and evolution of the Earth's continental crust. Journal of Australian Geology & Geophysics 17, 55-62.

Tröger, W.E., 1982. Optische Bestimmung der gesteinsbildenden Minerale, Teil 2. Schweizbart'sche Verlagsbuchhandlung, Stuttgart, 822 pp.

van Bemmelen, R.W., 1949. The Geology of Indonesia. Government Printing Office, The Hague (3 volumes).

van Leeuwen, T.M., Taylor, R., Coote, A., Longstaffe, F.J., 1994. Porphyry molybdenum mineralization in a continental collision setting at Malala, northwest Sulawesi, Indonesia. Journal of Geochemical Exploration 50, 279-315.

van Leeuwen, T.M., Muhardjo, 2005. Stratigraphy and tectonic setting of the Cretaceous and Paleogene volcanic-sedimentary successions in northwest Sulawesi, Indonesia: implications for the Cenozoic evolution of Western and Northern Sulawesi. Journal of Asian Earth Sciences 25, 481-511.

van Leeuwen, T.M., Allen, C.M., Kadarusman, A., Elburg, M., Palin, J.M., Muhardjo, Suwijanto, 2007. Petrologic, isotopic, and radiometric age constraints on the origin and tectonic history of the Malino Metamorphic Complex, NW Sulawesi, Indonesia. Journal of Asian Earth Sciences 29, 5-6, 751-777.

van Leeuwen, T.M., Allen, C.M., Elburg, M., Massonne, H.-J., Palin, J.M., Hennig, J., 2016. The Palu Metamorphic Complex, NW Sulawesi, Indonesia: Origin and evolution of a young metamorphic terrane with links to Gondwana and Sundaland. Journal of Asian Earth Sciences 115, 133-152.

Viete, D.R., Richards, S.W., Lister, G.S., Oliver, G.J.H., Banks, G.J., 2010. Lithospheric-scale extension during Grampian orogenesis in Scotland. Geological Society of London Special Publications 335, 121-160.

Weissel, J.K., 1980. Evidence for Eocene oceanic crust in the Celebes Basin. In: Hayes, D.E. (Ed.), The Tectonic and Geologic Evolution of South-east Asian Seas and Islands. American Geophysical Union Monograph 23, 37-48.

Whitney, D.L., Teyssier, C., Rey, P., Buck, W.R., 2013. Continental and oceanic core complexes. Geological Society of America Bulletin 125, 273-298.

Wijbrans, J.R., McDougall, I., 1986. $^{40}Ar/^{39}Ar$ dating of white micas from an Alpine high-pressure metamorphic belt on Naxos (Greece): the resetting of the argon isotopic system. Contributions to Mineralogy and Petrology 93, 187-194.

Wolf, R.A., Farley, K.A., Silver, L.T., 1996. Helium diffusion and low-temperature thermo-chronometry of apatite. Geochimica et Cosmochimica Acta 60**,** 4231–4240.

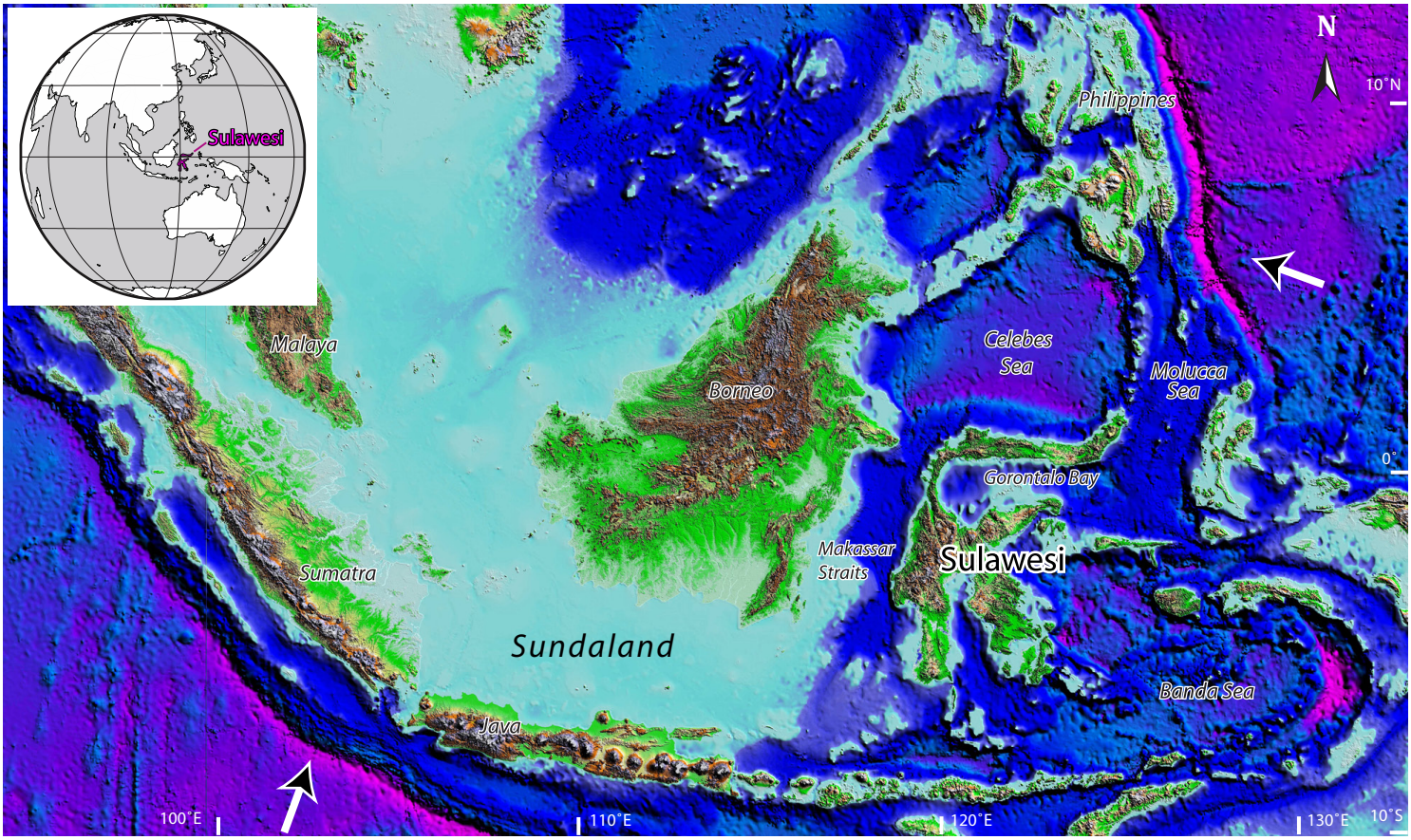

Fig. 1: Map of the Shuttle Radar Topography Mission (SRTM) including bathymetry data of SE Asia. Areas in light blue are continental shelf regions. Dark blue to pink areas represent deep ocean floor. Arrows indicate the plate velocities with respect to the Eurasian plate based on Socquet et al. (2006).

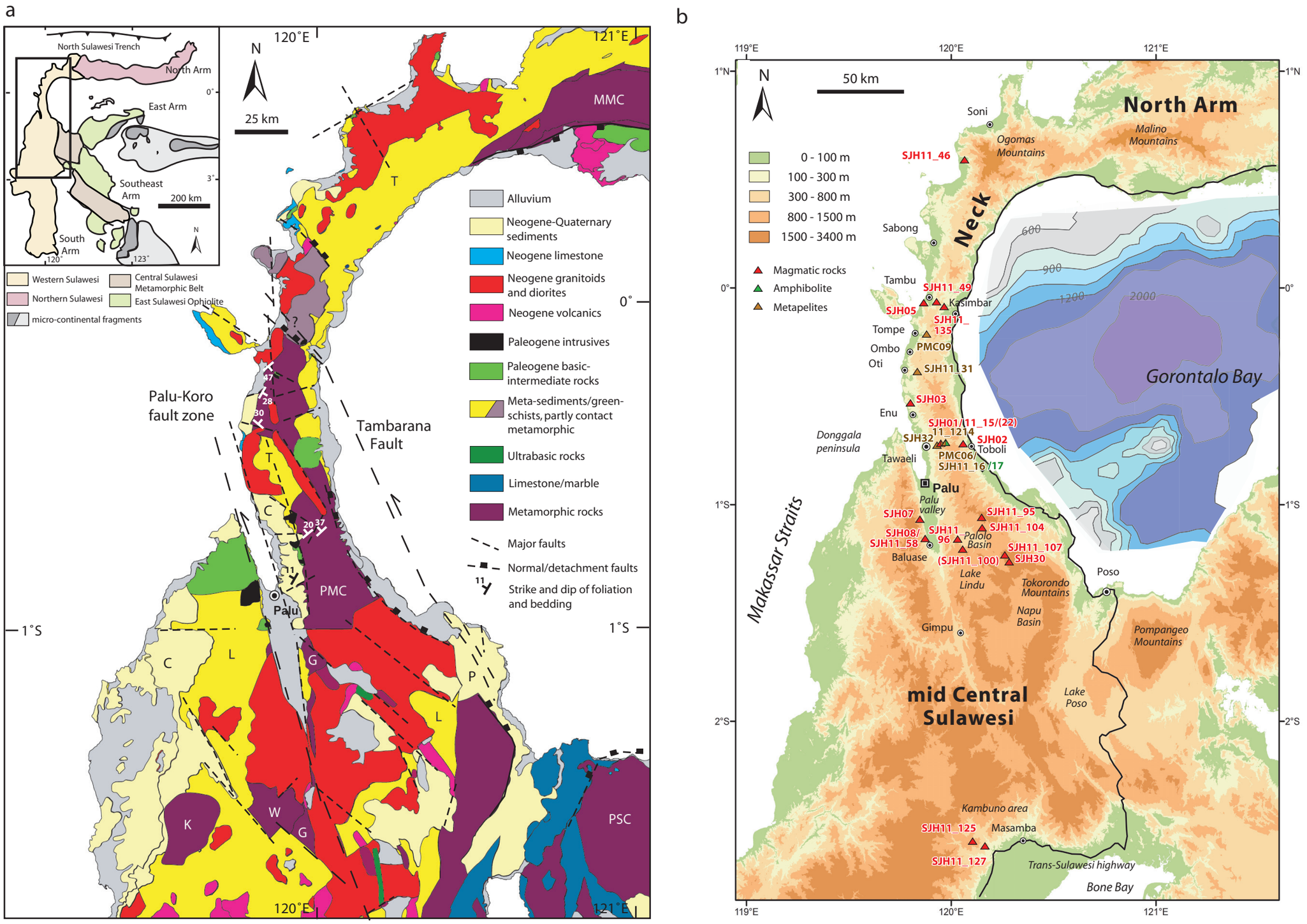

Fig. 2: Overview maps of west Central Sulawesi. a) Geological map of west Central Sulawesi based on Sukamto (1973), Ratman (1976), Simandjuntak et al. (1991, 1997), Sukido et al. (1993), van Leeuwen & Muhardjo (2005), Calvert & Hall (2007), Pholbud et al. (2012) and own field observations. Small inset map shows the main tectono-stratigraphic provinces. PMC - Palu Metamorphic Complex, MMC - Malino Metamorphic Complex, G - Gumbasa Metamorphic Complex, K - Karossa Metamorphic Complex, W - Wana Metamorphic Complex, PSC - Pompangeo Schist Complex, T - Tinombo Formation, L - Latimojong Formation, C - Celebes Molasse, P - Puna Formation. b) Bathymetry map of Gorontalo Bay based on Jablonski et al. (2007), and digital elevation map of west Central Sulawesi showing selected towns, regions and sample locations.

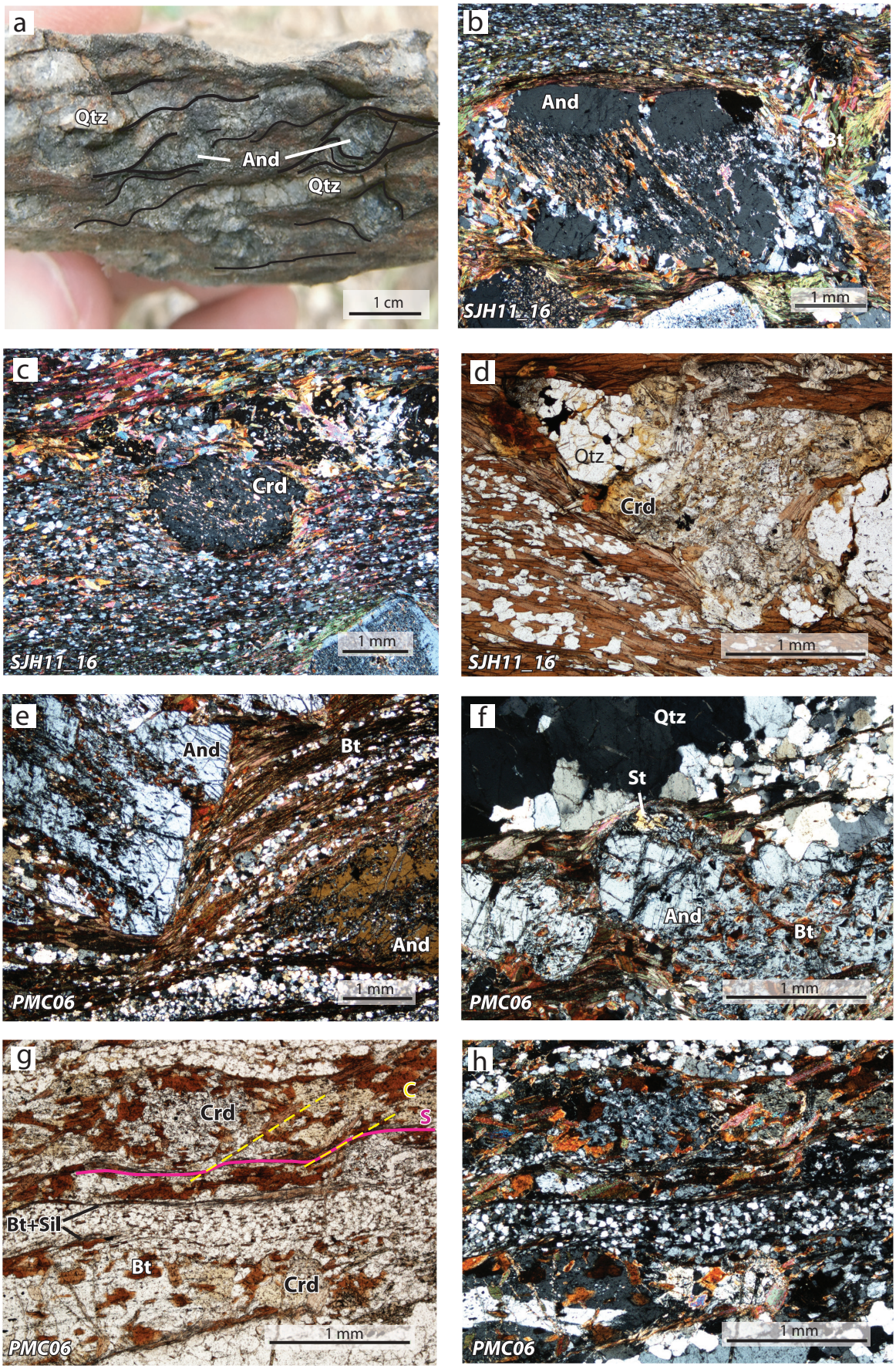

Fig. 3: Photos of hand specimen (a) and thin sections (b-h) of biotite schists from the southern PMC. a) Schist with shear bands around andalusite crystals. b, c) Andalusite and cordierite porphyroblasts with aligned inclusions from an earlier foliation (XPL). d) Quartz lens with pinitised cordierite (PPL). e) Strong foliation of quartz/feldspar and biotite surrounding andalusite porphyroblasts (XPL). f) Small xenoblastic staurolite in contact with andalusite surrounded by the foliation (XPL). g, h) Bands of cordierite and biotite which are cut by small shear bands of biotite and fibolitic sillimanite (PPL, XPL). PPL - plane polarised light; XPL - crossed polarised light.

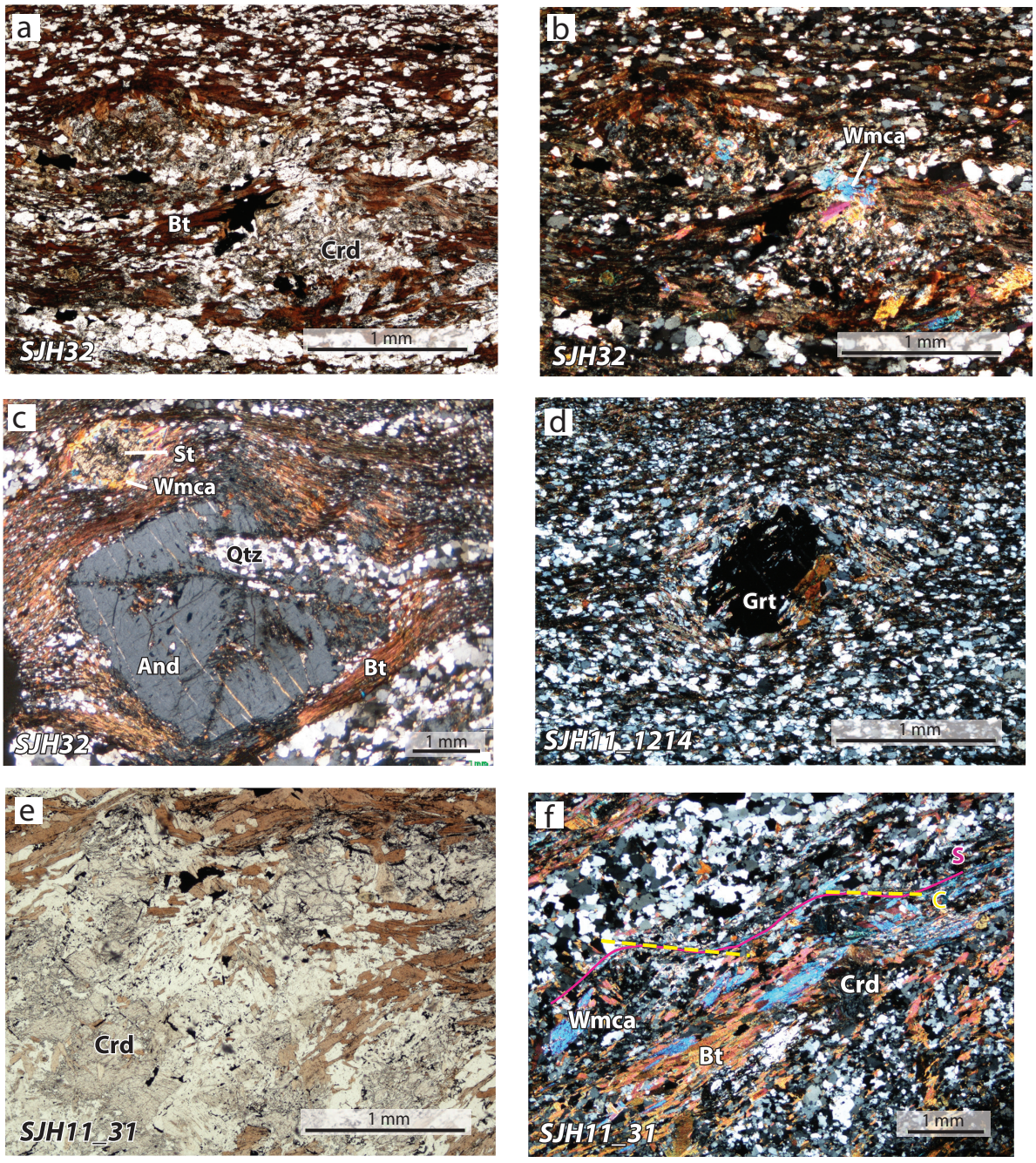

Fig. 4: Photomicrographs of biotite schists from the southern PMC (a-d) and biotite - white mica schists from the northern PMC (e, f). a, b) Pinitised cordierite surrounded by biotite of the foliation and partly overgrown by white mica during retrograde metamorphism (PPL, XPL). c) Andalusite and staurolite porphyroblasts wrapped by the dominant foliation. Staurolite is rimmed and partly replaced by white mica (XPL). d) Garnet porphyroblast with aligned quartz, feldspar and biotite inclusions indicating growth during an earlier event (XPL). e) Cordierite which is partly altered to pinite (PPL). f) SC shear fabric formed by biotite and white mica (XPL).

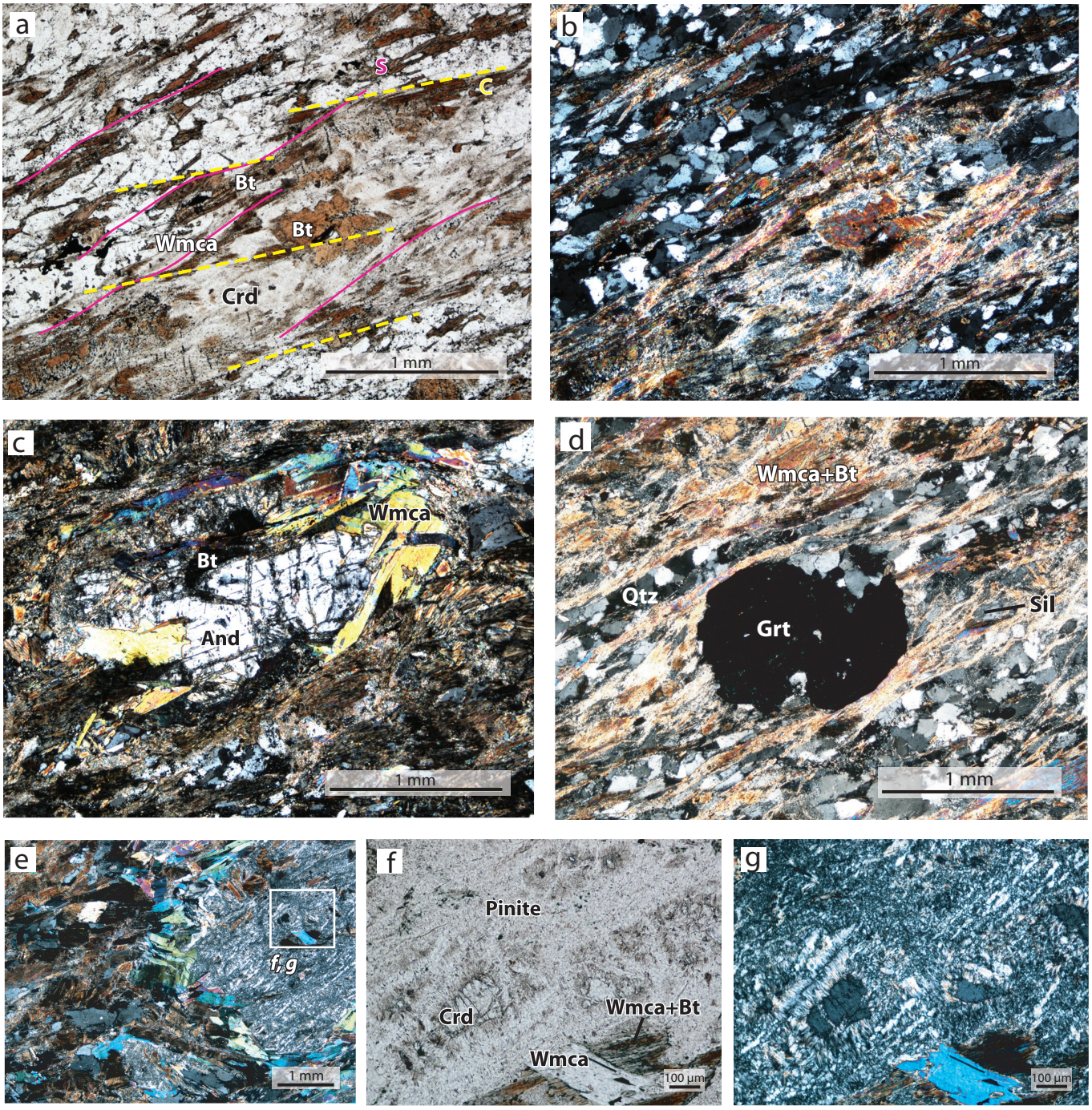

Fig. 5: Photomicrographs of biotite - white mica schist (PMC09) from the northern PMC. a, b) Strongly pinitised cordierite with biotite surrounded by an SC shear fabric of biotite and white mica (PPL, XPL). c) Andalusite porphyroblast in contact with biotite and partly rimmed by hypidiomorphic white mica (XPL). d) Garnet porphyroblast within SC shear fabric of biotite - white mica and subordinate fibrolitic sillimanite (XPL). e-g) Pinite pseudomorph after cordierite with biotite - white mica intergrowth which is overgrown by younger hypidiomorphic white mica that also grew at the rim of the pseudomorph during retrograde metamorphism (XPL, PPL, XPL).

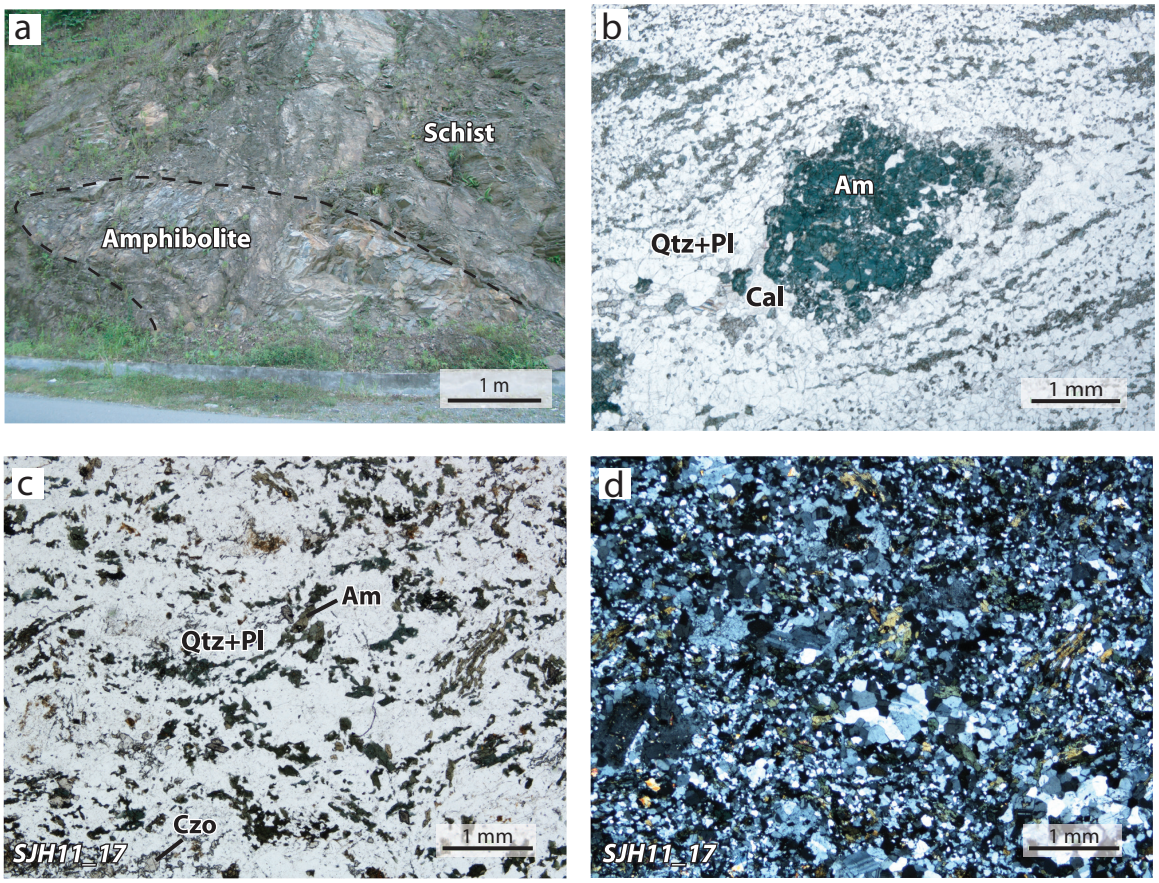

Fig. 6: Outcrop photo (a) and photomicrographs (b-d) of amphibolites from the southern PMC. a) Sharp contact between an amphibolite lens and biotite schist. b) Fine-grained mylonitic amphibolite with green-bluish amphibole porphyroclasts (PPL). c, d) Fine-grained recrystallised amphibolite with (quartz-) plagioclase relicts surrounded by amphiboles forming a weak fabric (PPL, XPL).

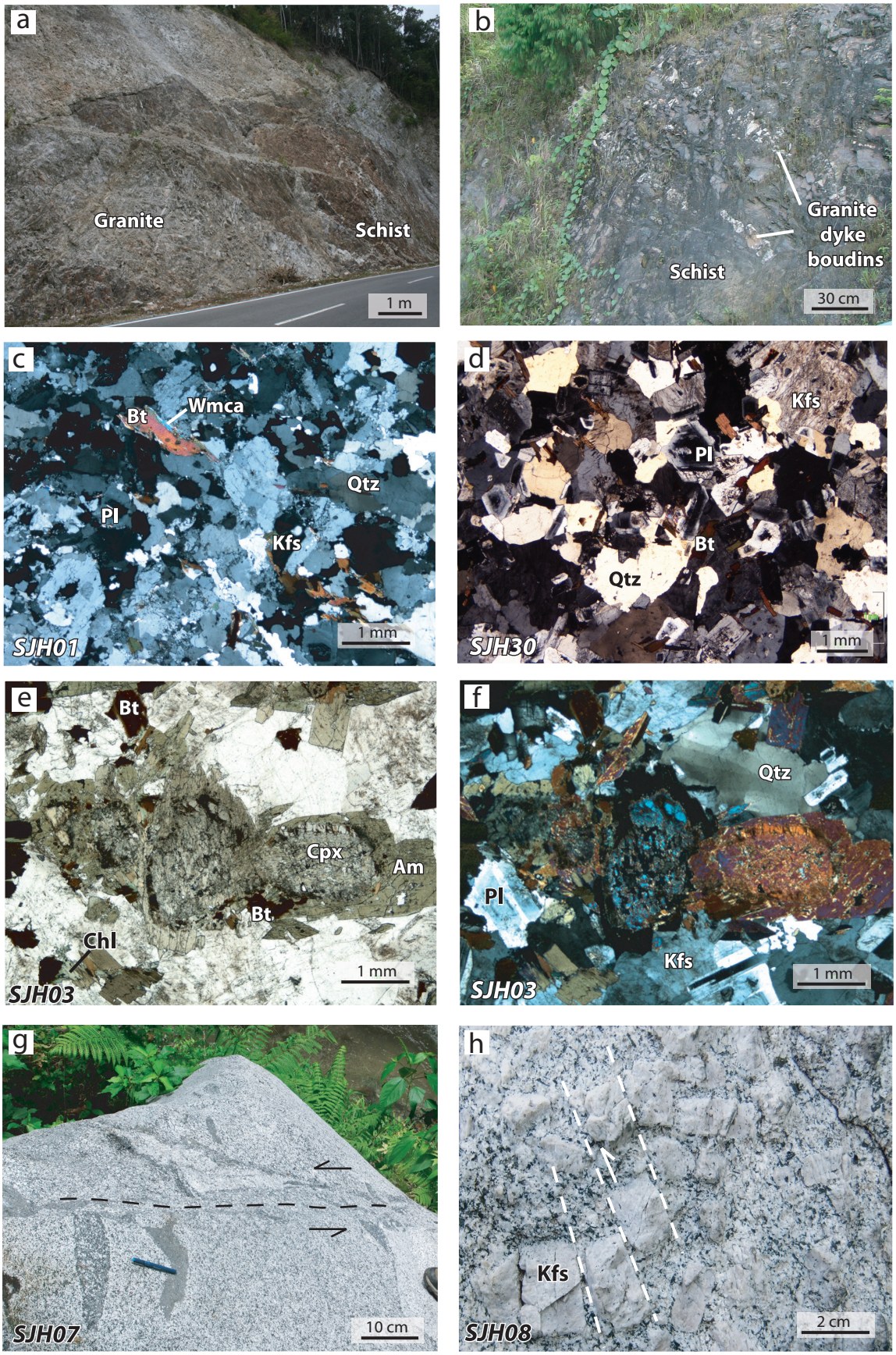

Fig. 7: Outcrop photos and photomicrographs of Neogene S-type (a-d) and I-type (e-h) granitoids or diorites of west Central Sulawesi. a) Granite having intruded the schists of the PMC. b) Boudinage of granite dykes sub-parallel to the schist foliation. c) Undeformed granite dyke with hypidiomorphic and xenomorphic biotites, as well as subordinate white mica (XPL). d) Granite with abundant hypidiomorphic biotites showing no orientation (XPL). e, f) Coarse-grained granodiorite with relict clinopyroxene cores which are mantled by amphiboles (PPL, XPL). g) Small shear zone in diorite boulder. h) Granodiorite boulder showing small-scale brittle faulting in K-feldspar megacrysts.

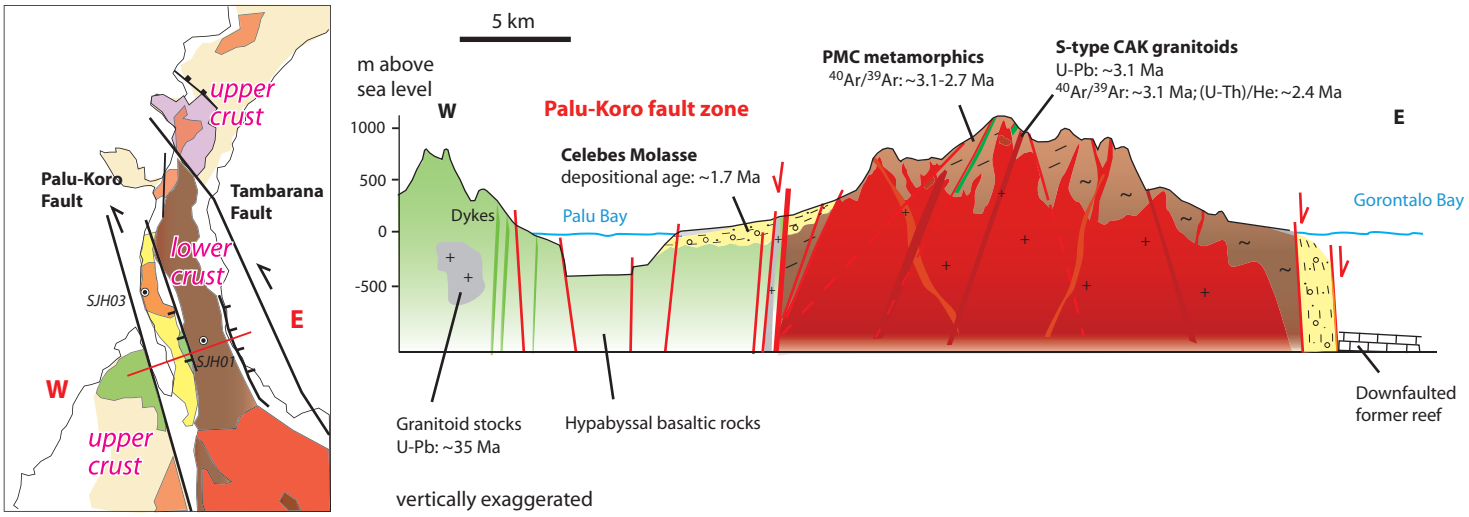

Fig. 8: Cross-section through the Neck and Donggala peninsula highlighting the fast exhumation of mid to lower crustal rocks of the PMC which is located in a normal fault-dominated system between the major Palu-Koro and Tambarana strike-slip faults.

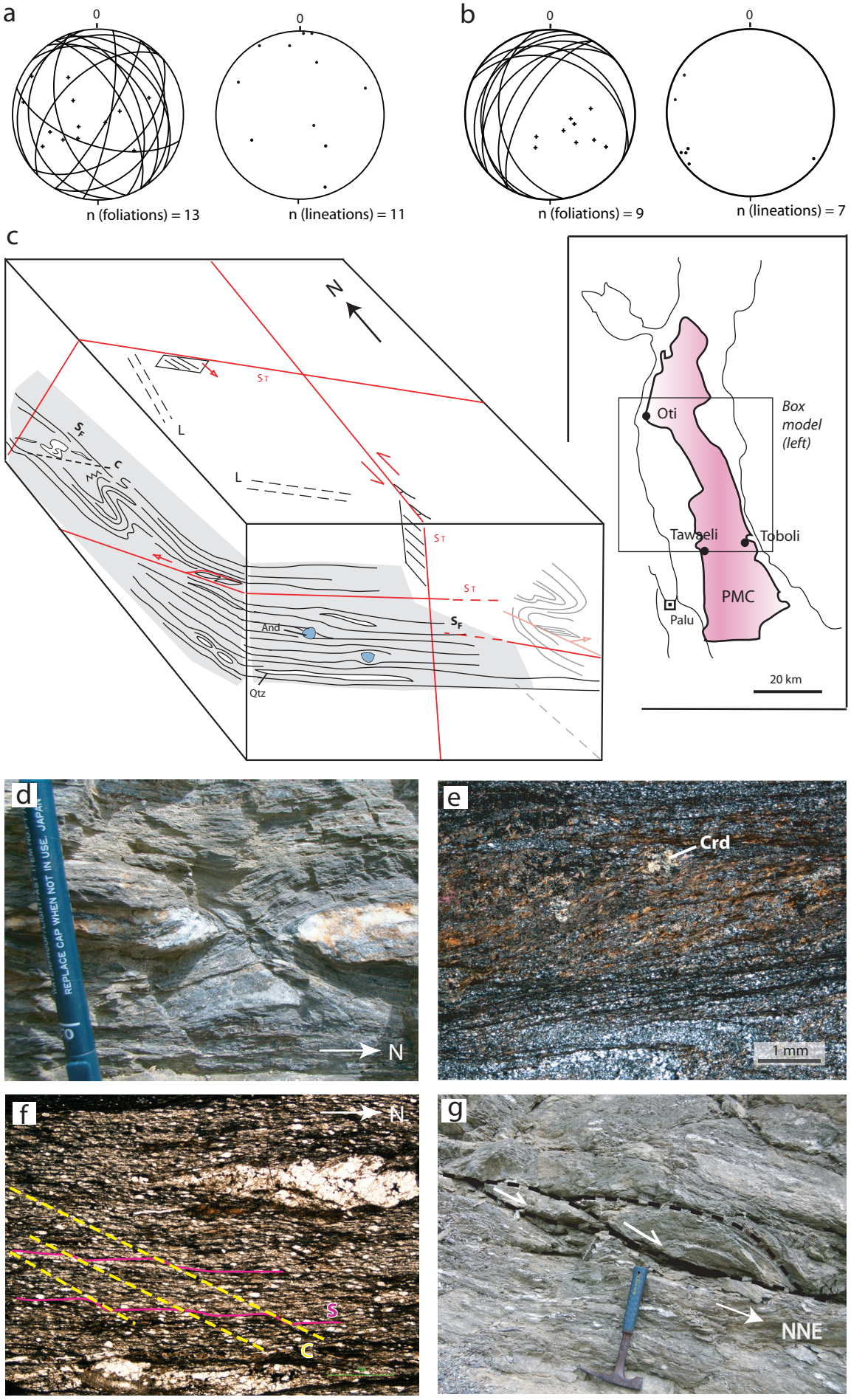

Fig. 9: Structural features of the PMC. a, b) Stereonet diagrams for foliations and lineations of the northern (a) and southern (b) PMC (equal area projection, lower hemisphere). c) Sketch box model summarising the structural features of the PMC. S_F - foliation; L - stretching lineation; C - crenulation cleavage; S_T - fault; And - andalusite; Qtz - quartz. d) Quartz vein boudinage indicating ~N-S extension. e) Meso-mylonitic biotite hornfels showing small contact metamorphic cordierite that is surrounded by shear bands (XPL). f) Proto-mylonitic slate showing a well developed SC shear fabric (XPL). g) Low-angle N-dipping normal fault with detached schist fragments, indicating extensional dip-slip movement.

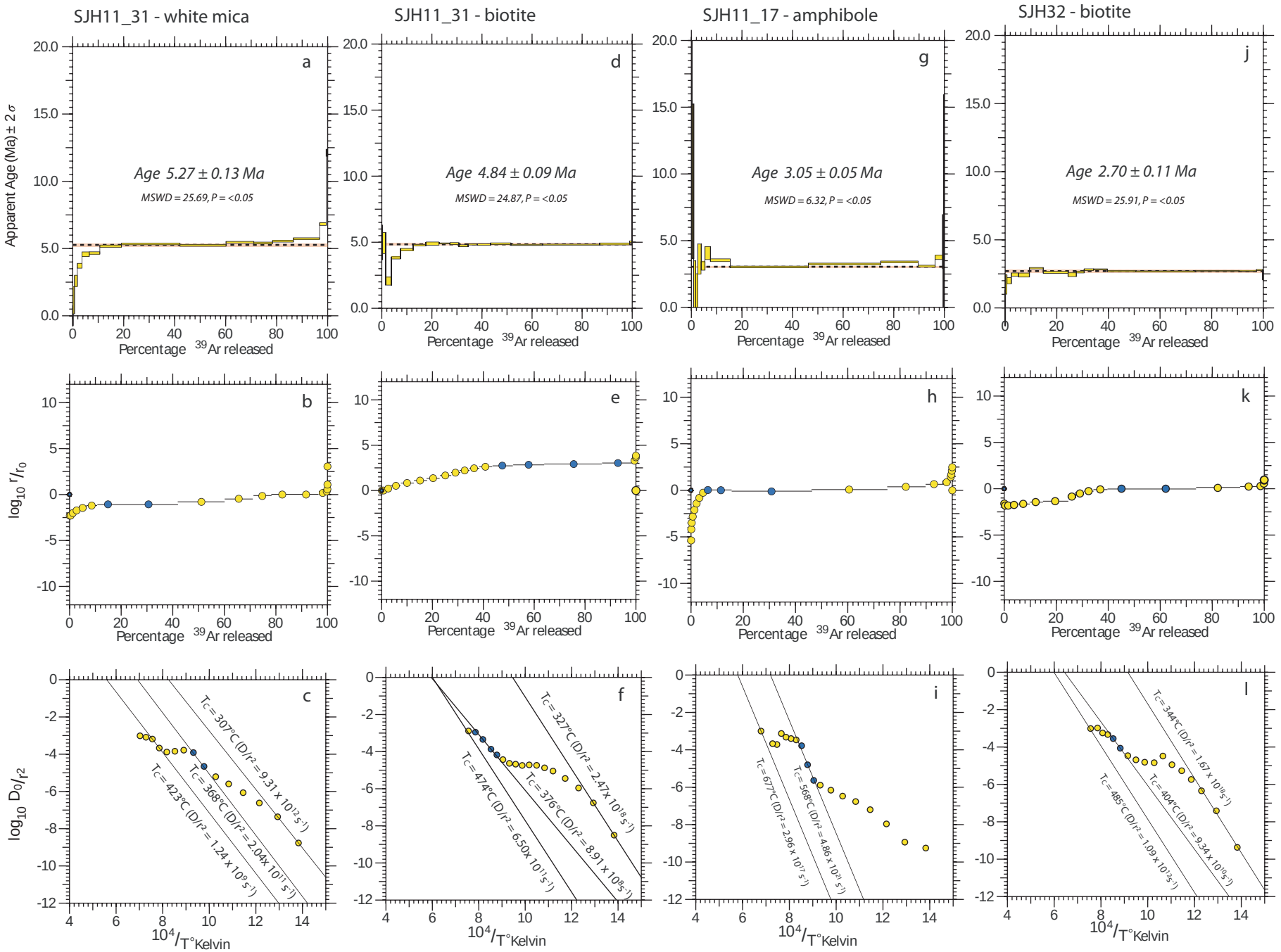

Fig. 10: Apparent age diagrams *(a, d, g, j,)*, $\log_{10}(r/r_0)$ plots *(b, e, h, k)* and Arrhenius plots *(c, f, i, l)* for $^{40}Ar/^{39}Ar$ step-heating experiments of metamorphic rocks. Age plateaux are highlighted in the age spectra; the $\log_{10}(r/r_0)$ plots are used to identify meaningful domains which are related to closure temperatures as indicated from the Arrhenius plots.

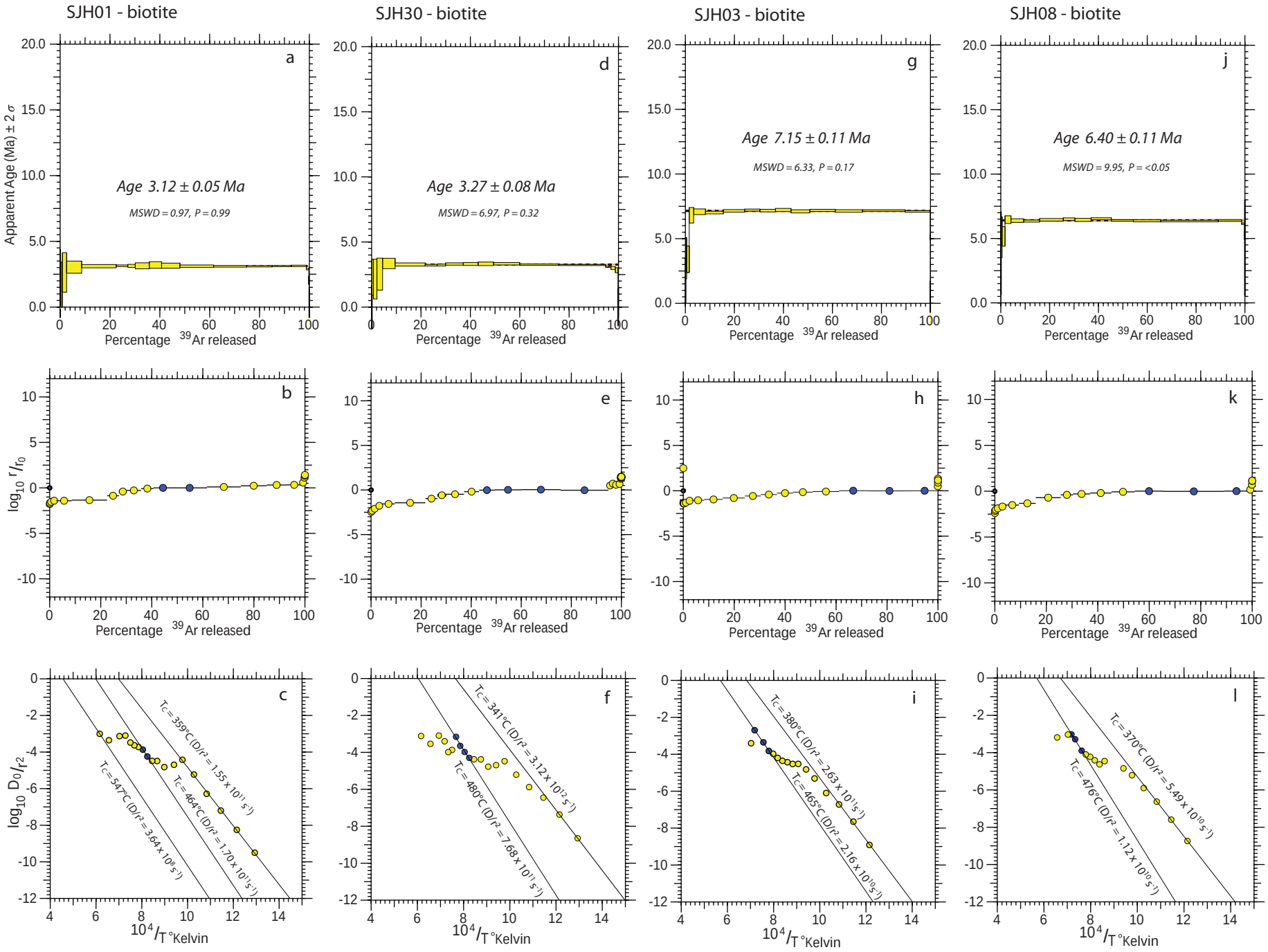

Fig. 11: Apparent age diagrams *(a, d, g, j,)*, $\log_{10}(r/r_0)$ plots *(b, e, h, k)* and Arrhenius plots *(c, f, i, l)* for $^{40}Ar/^{39}Ar$ step-heating experiments of magmatic rocks. Age plateaux are highlighted in the age spectra; the $\log_{10}(r/r_0)$ plots are used to identify meaningful domains which are related to closure temperatures as indicated from the Arrhenius plots.

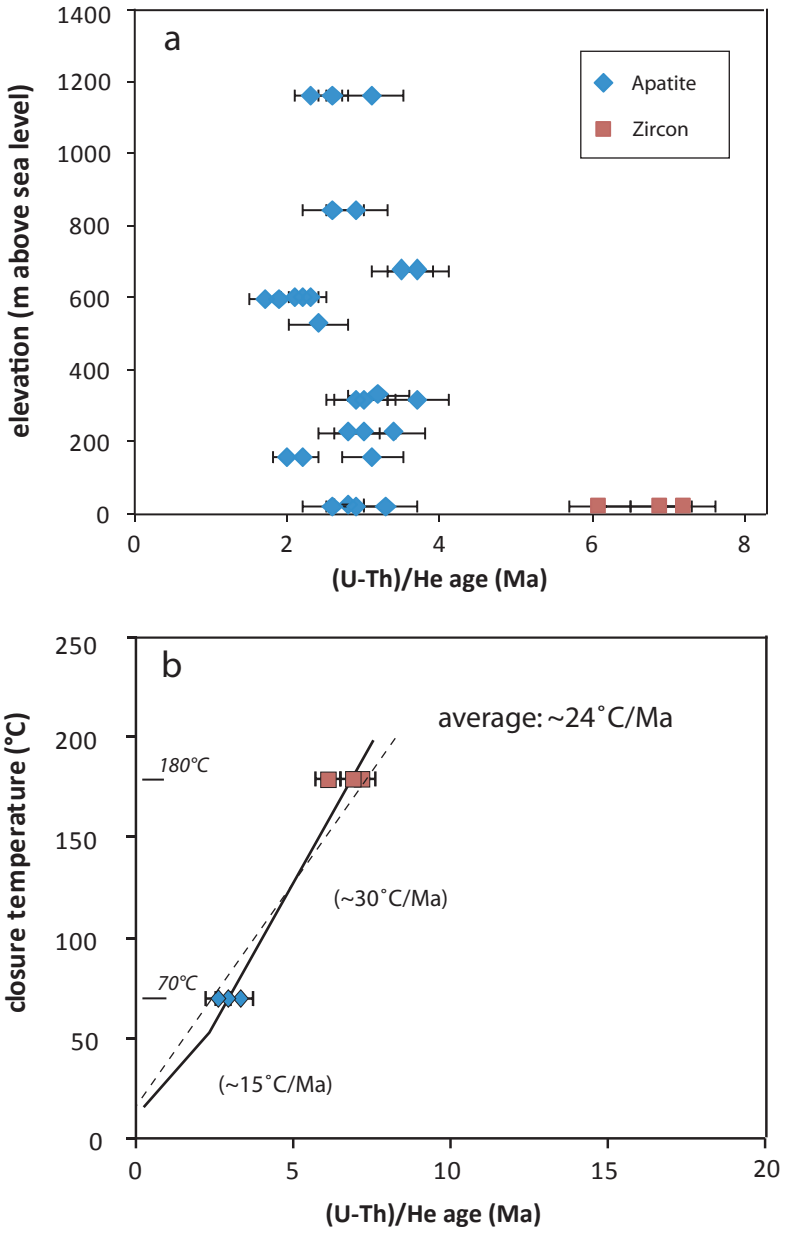

Fig. 12: Summary of apatite and zircon (U-Th)/He ages. a) Age-elevation relationship of all analyses, indicating rapid exhumation. b) Low-temperature cooling path of sample SJH03.

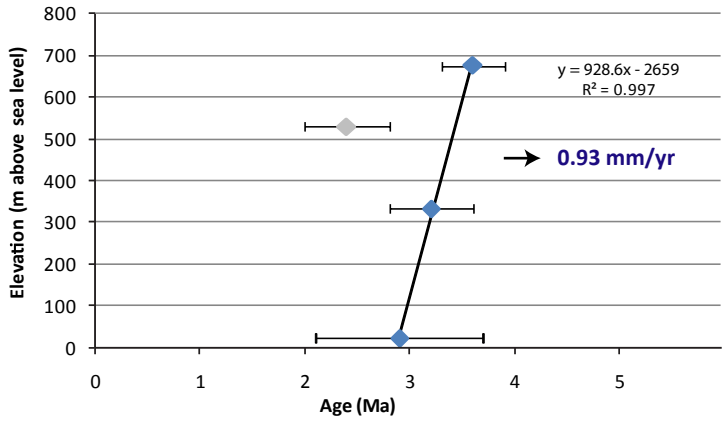

Fig. 13: Apatite (U-Th)/He age-elevation plot from a profile line between Tawaeli and Toboli (Fig. 2b) across the southern PMC.

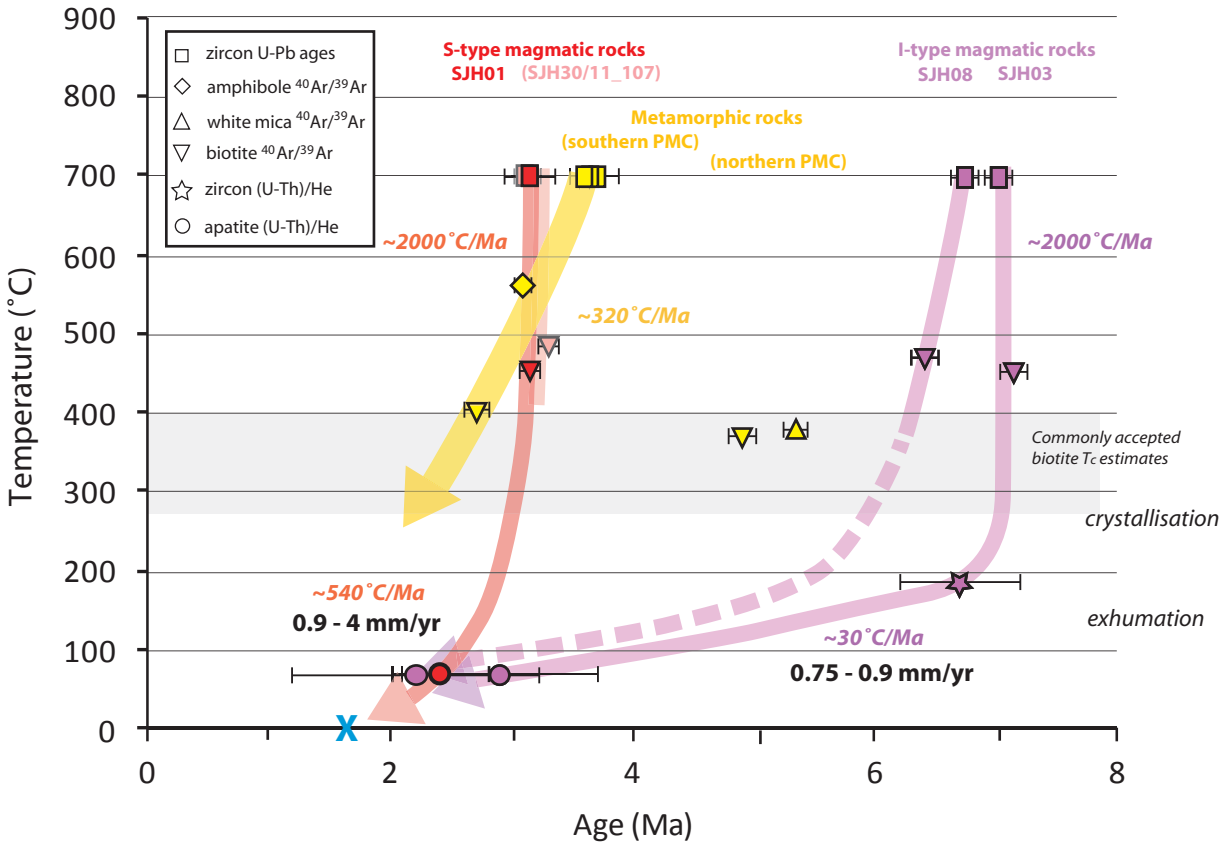

Fig. 14: Cooling paths of magmatic (red/pink) and metamorphic rocks (yellow) of the Neck and mid Central Sulawesi. The blue cross marks the depositional age of 1.7 Ma reported for the Celebes Molasse by van Leeuwen & Muhardjo (2005). The mid crustal metamorphic rocks and intruded S-type granitoids show very fast cooling to the near-surface during the Pliocene, indicating rapid exhumation. In contrast, upper crustal Late Miocene I-type rocks show rapid cooling at shallow depths and significantly slower cooling than the metamorphics and S-type granitoids during exhumation. Range of commonly accepted biotite closure temperature (T_C) estimates after Harrison et al. (1985) and Grove & Harrison (1996).

Tab. 1.1: (U-Th)/He apatite data from granitoids, west Central Sulawesi.

Sample No.	Elevation (m above sea level)	Lab ID	He No.	No. of grains analysed	^{4}He (ncc)	Mass (mg)	^{a}F$_T$	U ppm	Th ppm	Sm ppm	Th/U	^{b}[eU] ppm	Uncorrected age (Ma)	Corrected age (Ma)	Error (Ma) ±1σ	Grain length (μm)	^{c}Grain radius (μm)	^{d}SD	^{e}Grain morphology
SJH01	529	6727	19776	2	0.035	0.0094	0.74	8.5	16.7	133.6	1.97	12.4	1.8	**2.4**	**0.2**	150.0	73.5	18.8	0T
SJH01	529	6728	19765	1	0.085	0.0021	0.66	15.8	54.6	174.5	3.46	28.6	7.5	^{f}**11.4**	**0.7**	166.9	43.1	-	1T
SJH02	333	6730	19761	2	0.050	0.0093	0.75	7.2	25.7	175.0	3.55	13.2	2.4	**3.2**	**0.2**	163.6	58.1	3.4	1T
SJH03	22	6733	19737	1	0.053	0.0016	0.63	57.7	99.8	330.4	1.73	81.2	2.1	**3.3**	**0.2**	89.1	42.5	-	0T
SJH03	22	6734	19748	1	0.068	0.0018	0.67	71.4	143.3	498.0	2.01	105.1	2.0	**2.9**	**0.2**	132.0	46.7	-	1T
SJH03	22	6735	19750	1	0.052	0.0017	0.65	61.6	138.9	395.4	2.25	94.2	1.7	**2.6**	**0.2**	143.0	42.2	-	0T
SJH05	27	7388	21834	2	0.078	0.0153	0.78	10.9	17.2	209.6	1.58	14.9	2.2	**2.8**	**0.2**	173.9	74.1	0.6	1T
SJH05	27	7438	21869	2	0.412	0.0212	0.80	23.7	39.7	234.0	1.68	33.0	3.8	^{f}**4.8**	**0.3**	212.1	68.5	12.0	0T
SJH08	159	7385	21828	1	0.161	0.0076	0.76	49.9	124.7	253.0	2.50	79.2	1.7	**2.2**	**0.1**	112.0	56.0	-	0T
SJH08	159	7386	21830	1	0.109	0.0035	0.71	32.2	37.4	187.5	1.16	41.0	4.3	^{f}**6.1**	**0.4**	98.8	49.5	-	0T
SJH08	159	7387	21832	1	0.143	0.0037	0.71	24.7	43.1	203.4	1.75	34.8	6.5	^{f}**9.1**	**0.6**	101.2	50.6	-	0T
SJH08	159	7577	22299	1	0.042	0.0080	0.78	12.5	39.1	174.5	3.12	21.7	1.6	**2.0**	**0.1**	191.2	64.4	-	0T
SJH08	159	7578	22301	1	0.136	0.0081	0.78	27.5	70.1	193.4	2.55	44.0	2.4	**3.1**	**0.2**	274.0	65.1	-	1T
SJH11_15	675	7376	21813	1	0.065	0.0145	0.82	7.7	11.4	89.6	1.49	10.4	2.9	**3.5**	**0.2**	169.8	84.9	-	0T
SJH11_15	675	7378	21816	1	0.570	0.0162	0.82	4.3	25.8	89.3	6.03	10.4	22.7	^{f}**27.6**	**1.7**	177.1	88.6	-	0T
SJH11_15	675	7433	21859	3	0.133	0.0161	0.75	8.6	40.4	96.7	4.73	18.1	2.8	**3.7**	**0.2**	141.7	61.6	4.8	2T
SJH11_15	675	7434	21861	3	0.133	0.0122	0.72	9.9	23.5	86.0	2.37	15.4	4.2	^{f}**5.8**	**0.4**	127.1	56.4	1.3	0T
SJH11_15	675	7569	22317	1	0.099	0.0083	0.78	8.8	31.1	90.6	3.53	16.1	4.7	^{f}**6.0**	**0.4**	163.6	71.0	-	0T
SJH11_22	454	7382	21822	1	0.075	0.0086	0.78	9.4	24.2	118.3	2.57	15.1	3.6	^{f}**4.6**	**0.3**	136.6	68.3	-	0T
SJH11_22	454	7383	21824	1	0.198	0.0050	0.74	14.4	51.4	222.9	3.56	26.5	8.9	^{f}**12.1**	**0.8**	117.7	58.9	-	0T
SJH11_22	454	7439	21871	2	0.043	0.0094	0.70	14.1	44.6	174.8	3.17	24.6	1.1	^{f}**1.5**	**0.1**	150.2	48.5	4.4	0T
SJH11_22	454	7576	22297	1	0.054	0.0027	0.66	8.6	24.9	150.5	2.89	14.5	7.5	^{f}**11.3**	**0.7**	139.6	43.8	-	0T
SJH11_49	229	7407	21918	1	0.053	0.0135	0.83	11.0	1.6	121.2	0.14	11.4	2.3	**2.8**	**0.2**	168.7	84.4	-	0T
SJH11_49	229	7408	21927	1	0.079	0.0049	0.79	27.1	4.4	196.8	0.16	28.1	3.7	^{f}**4.7**	**0.3**	136.8	68.4	-	1T
SJH11_49	229	7567	22321	2	0.027	0.0041	0.67	17.1	2.6	180.7	0.15	17.7	2.0	**3.0**	**0.2**	122.2	41.8	7.7	0T
SJH11_49	229	7568	22319	2	0.232	0.0133	0.78	15.5	1.5	113.9	0.10	15.9	7.0	^{f}**9.0**	**0.6**	181.2	60.3	0.2	0T
SJH11_49	229	7511	22196	2	0.126	0.0119	0.78	24.5	2.5	192.8	0.10	25.1	2.7	**3.4**	**0.2**	200.3	62.8	17.7	1T
SJH11_58	318	7391	21841	1	0.155	0.0115	0.79	23.6	59.9	110.1	2.53	37.7	2.3	**2.9**	**0.2**	117.7	58.9	-	0T
SJH11_58	318	7392	21884	1	0.304	0.0106	0.80	15.5	26.8	1.0	1.73	21.8	8.6	^{f}**10.7**	**0.7**	140.5	70.3	-	0T
SJH11_58	318	7393	21886	1	0.251	0.0041	0.72	85.8	204.5	364.0	2.38	133.9	2.7	**3.7**	**0.2**	104.3	52.2	-	0T
SJH11_58	318	7565	22331	2	0.124	0.0059	0.71	38.2	84.7	142.1	2.22	58.1	2.1	**3.0**	**0.2**	138.6	47.9	8.1	1T
SJH11_95	1160	7373	21807	2	0.094	0.0154	0.77	4.4	22.4	166.2	5.08	9.7	3.9	^{f}**5.1**	**0.3**	156.6	69.2	8.8	0T
SJH11_95	1160	7374	21809	1	0.459	0.0056	0.75	15.5	35.4	343.2	2.28	23.8	20.7	^{f}**27.6**	**1.7**	122.1	61.1	-	0T
SJH11_95	1160	7437	21867	1	0.268	0.0381	0.87	15.2	41.2	247.0	2.71	24.9	2.0	**2.3**	**0.1**	228.8	114.4	-	0T
SJH11_95	1160	8272	24314	1	0.043	0.0094	0.79	7.8	31.1	236.4	3.96	15.1	2.4	**3.1**	**0.2**	198.8	68.5		1T
SJH11_95	1160	8273	24312	1	0.020	0.0046	0.71	8.2	48.4	158.2	5.94	19.6	1.8	**2.6**	**0.1**	219.7	45.4		1T
SJH11_96	603	7395	21890	1	0.054	0.0196	0.83	7.0	15.7	159.6	2.24	10.7	1.7	**2.1**	**0.1**	160.1	80.1	-	0T
SJH11_96	603	7570	22315	2	0.041	0.0093	0.73	9.9	27.2	180.1	2.74	16.3	1.6	**2.2**	**0.1**	201.2	52.6	0.5	0T
SJH11_96	603	7571	22305	1	0.127	0.0517	0.88	4.7	16.4	73.8	3.52	8.6	2.1	**2.3**	**0.1**	242.0	145.7	-	0T
SJH11_96	603	7509	22210	2	0.240	0.0164	0.79	11.2	20.3	218.3	1.82	16.0	5.9	^{f}**7.4**	**0.5**	187.5	74.0	3.1	1T
SJH11_96	603	7510	22198	2	0.081	0.0060	0.70	10.6	20.5	211.8	1.94	15.4	5.0	^{f}**7.1**	**0.4**	144.0	48.5	6.8	1T
SJH11_100	994	7403	21911	1	0.098	0.0074	0.74	8.6	8.2	90.8	0.95	10.5	7.6	^{f}**10.3**	**0.6**	106.5	53.3	-	2T
SJH11_100	994	7404	21913	1	0.151	0.0044	0.73	34.8	24.3	328.6	0.70	40.5	5.1	^{f}**7.0**	**0.4**	97.2	48.6	-	1T
SJH11_100	994	7405	21915	1	0.067	0.0054	0.78	25.6	15.1	279.2	0.59	29.1	2.7	^{f}**3.5**	**0.2**	136.8	68.4	-	1T
SJH11_100	994	7574	22294	1	2.917	0.0052	0.74	32.0	210.6	193.5	6.57	81.5	41.5	^{f}**56.4**	**3.5**	155.8	57.5	-	0T
SJH11_100	994	8269	24304	1	0.025	0.0016	0.66	36.0	28.5	320.9	0.79	42.7	3.0	^{f}**4.5**	**0.2**	128.6	44.3	-	1T
SJH11_100	994	8270	24306	1	0.102	0.0050	0.75	25.2	21.9	224.8	0.87	30.3	5.5	^{f}**7.3**	**0.3**	174.7	53.5	-	2T
SJH11_100	994	8271	24308	1	0.048	0.0164	0.82	8.8	27.9	262.6	3.15	15.4	1.5	^{f}**1.9**	**0.1**	214.8	87.3	-	0T
SJH11_104	844	7370	21794	1	0.083	0.0038	0.71	14.9	83.7	340.9	5.61	34.6	3.7	^{f}**5.1**	**0.3**	112.5	56.3	-	0T
SJH11_104	844	7371	21796	1	0.072	0.0062	0.77	19.7	52.5	341.7	2.67	32.0	2.2	**2.9**	**0.2**	130.8	65.4	-	1T
SJH11_104	844	7372	21805	1	0.059	0.0060	0.72	14.0	70.6	313.6	5.03	30.6	1.9	**2.6**	**0.2**	105.0	52.5	-	2T
SJH11_125	598	7411	21934	3	0.097	0.0144	0.76	26.5	12.6	186.5	0.48	29.5	1.4	**1.9**	**0.1**	165.7	60.0	9.8	1T
SJH11_125	598	7507	22190	1	0.083	0.0068	0.79	39.2	76.6	513.3	1.95	57.2	1.4	**1.7**	**0.1**	205.4	71.9	-	1T
SJH11_125	598	7508	22212	2	0.122	0.0134	0.77	19.3	11.6	158.7	0.60	22.0	2.6	^{f}**3.4**	**0.2**	205.5	56.5	11.8	0T
SJH11_127	174	7400	21905	2	0.145	0.0038	0.70	94.0	177.9	917.2	1.89	135.8	1.6	**2.3**	**0.1**	185.8	56.0	0.9	2T
SJH11_127	174	7401	21907	1	0.127	0.0050	0.75	44.1	50.2	235.2	1.14	55.9	2.8	^{f}**3.7**	**0.2**	112.1	56.1	-	1T
SJH11_127	174	7512	22194	2	0.500	0.0390	0.84	15.5	20.3	111.5	1.32	20.3	4.3	^{f}**5.2**	**0.3**	262.9	93.0	20.4	1T
SJH11_135	141	7435	21863	4	0.073	0.0068	0.64	29.4	5.1	208.3	0.17	30.6	1.8	**2.9**	**0.2**	136.5	39.2	4.3	2T
SJH11_135	141	7380	21819	1	0.051	0.0062	0.76	26.8	5.4	309.1	0.20	28.1	1.8	**2.4**	**0.1**	124.3	62.2	-	2T

Tab. 1.2: (U-Th)/He zircon data from sample SJH03 from the Neck.

Sample No.	Elevation (m above sea level)	Lab ID	He No.	No. of grains analysed	^{4}He (ncc)	Mass (mg)	^{a}F$_T$	U ppm	Th ppm	Th/U	^{b}[eU] ppm	Uncorrected Age (Ma)	Age (Ma)	Error (Ma) ±1σ	Grain length (μm)	Grain radius (μm)	^{e}Grain morphology
SJH03	22	7274	20929	1	7.485	0.0072	0.79	1075.1	481.6	0.45	1188.3	5.7	**7.2**	**0.4**	225.8	50.3	2T
SJH03	22	7275	20932	1	9.327	0.0053	0.77	1678.8	1705.0	1.02	2079.4	5.3	**6.9**	**0.4**	190.0	49.1	2T
SJH03	22	7276	20962	1	10.539	0.0169	0.84	764.3	347.6	0.45	846.0	5.1	**6.1**	**0.4**	320.5	63.0	2T

[a]F$_T$ is the α-ejection correction after Farley et al. (1996).

[b]Effective uranium content [U ppm + 0.235 Th ppm].

[c]Where more than one grain has been analysed then the mass weighted average radius (MWAR) of apatite crystals measured in the aliquot analysed is given.

[d]Standard deviation of the MWAR is used as a guide for the 'tightness' of the range of single crystal radii picked from more than one grain within a sample.

[e]Grain morphology - 0T = no crystal terminations, 1T = one crystal termination and 2T = 2 crystal terminations.

[f]Age considered unreliable and is not discussed further - see text.

Tab. 2: Summary of the apatite (U-Th)/He weighted mean ages and exhumation rates calculated by using a mean elevation model.

Sample ID	Elevation (m above sea level)	Corrected age (Ma)	Error (± 2σ)	Weighted mean age (Ma) *	Error	MSWD	Regional weighted mean age (Ma) *	Error	MSWD	Mean elevation (m above sea level)	Z_S (m)	Exhumation rate (mm/a)	Error -	Error +
Southern Neck														
SJH01	529	2.4	0.4							560	2222	**0.93**	0.13	0.19
SJH02	333	3.2	0.4				**3.1**	0.4	5.6	556	2116	**0.66**	0.07	0.09
SJH03	22			2.9	0.8	2.4				164	2155	**0.74**	0.16	0.28
SJH11_15	675			3.6	0.3	0.5				620	2410	**0.67**	0.05	0.06
Central Neck														
SJH05	27	2.8	0.4							200	2124	**0.76**	0.04	0.20
SJH11_135	141			2.5	2.5	5.0	**2.7**	0.4	5.0	310	2084	**0.83**	0.38	-0.83
SJH11_49	229			3.1	0.8	2.3				232	2317	**0.75**	0.15	0.26
W of PKF														
SJH08	159			2.2	1.0	12.0	**2.5**	0.6	18.0	518	1848	**0.84**	0.15	1.00
SJH11_58	318			3.2	1.1	4.8				560	2097	**0.66**	0.11	0.46
S of Palolo Basin														
SJH11_96	603			2.2	0.1	1.0				848	1962	**0.89**	-0.07	0.16
N of Palolo Basin														
SJH11_104	844			2.8	1.9	1.1	**2.6**	0.4	4.3	902	2239	**0.80**	0.31	1.75
SJH11_95	1160			2.5	0.8	6.9				1210	2203	**0.88**	0.18	0.44
Kambuno area														
SJH11_127	174	2.3	0.2				**2.0**	0.8	9.3	494	1900	**0.83**	-0.06	0.23
SJH11_125	598			1.8	1.3	2.0				883	1849	**1.03**	0.34	3.23

* Weighted mean ages were calculated by using Isoplot 4.11 (Ludwig, 2003).
Weighted mean errors at 95% confidence interval.